

## Structural analysis and optimization of a tethered swept wing for airborne wind energy generation

Candade, Ashwin A.; Ranneberg, Maximilian; Schmehl, Roland

**DOI**

[10.1002/we.2469](https://doi.org/10.1002/we.2469)

**Publication date**

2020

**Document Version**

Final published version

**Published in**

Wind Energy

**Citation (APA)**

Candade, A. A., Ranneberg, M., & Schmehl, R. (2020). Structural analysis and optimization of a tethered swept wing for airborne wind energy generation. *Wind Energy*, 23(4), 1006-1025.  
<https://doi.org/10.1002/we.2469>

**Important note**

To cite this publication, please use the final published version (if applicable).  
Please check the document version above.

**Copyright**

Other than for strictly personal use, it is not permitted to download, forward or distribute the text or part of it, without the consent of the author(s) and/or copyright holder(s), unless the work is under an open content license such as Creative Commons.

**Takedown policy**

Please contact us and provide details if you believe this document breaches copyrights.  
We will remove access to the work immediately and investigate your claim.



RESEARCH ARTICLE

# Structural analysis and optimization of a tethered swept wing for airborne wind energy generation

Ashwin A. Candade<sup>1,2</sup> | Maximilian Ranneberg<sup>1</sup> | Roland Schmehl<sup>2</sup>

<sup>1</sup>Section Wind Energy, Delft University of Technology, Delft, The Netherlands  
<sup>2</sup>EnerKite GmbH, Berlin, Germany

**Correspondence**

Ashwin A. Candade, Section Wind Energy, Delft University of Technology, Delft, The Netherlands.  
Email: a.a.candade@tudelft.nl

**Present Address**

EnerKite GmbH, Ackerstraße 76, 13355 Berlin, Germany

**Funding information**

H2020 Industrial Leadership, Grant/Award Number: H2020-FTIPilot-691173; H2020 Marie Skłodowska-Curie Actions, Grant/Award Number: AWECO H2020-ITN-642682

## Abstract

In this paper, we present an aero-structural model of a tethered swept wing for airborne wind energy generation. The carbon composite wing has neither fuselage nor actuated aerodynamic control surfaces and is controlled entirely from the ground using three separate tethers. The computational model is efficient enough to be used for weight optimisation at the initial design stage. The main load-bearing wing component is a nontypical “D”-shaped wing-box, which is represented as a slender carbon composite shell and further idealised as a stack of two-dimensional cross section models arranged along an anisotropic one-dimensional beam model. This reduced 2+1D finite element model is then combined with a nonlinear vortex step method that determines the aerodynamic load. A bridle model is utilised to calculate the individual forces as a function of the aerodynamic load in the bridle lines that connect the main tether to the wing. The entire computational model is used to explore the influence of the bridle on the D-box structure. Considering a reference D-box design along with a reference aerodynamic load case, the structural response is analysed for typical bridle configurations. Subsequently, an optimisation of the internal geometry and laminate fibre orientations is carried out using the structural computation models, for a fixed aerodynamic and bridle configuration. Aiming at a minimal weight of the wing structure, we find that for the typical load case of the system, an overall weight savings of approximately 20% can be achieved compared with the initial reference design.

## KEYWORDS

airborne wind energy, EnerKite, optimisation, structural modelling

## 1 | INTRODUCTION

Airborne wind energy (AWE) is an innovative technology that uses lightweight tethered flying devices to harvest wind energy at altitudes higher than conventional wind turbines. Of the two fundamental concepts, onboard and ground-based energy conversion,<sup>1</sup> we consider in this study the latter, specifically, an implementation that is based on a tethered wing operated in cyclic flight patterns which drive a set of ground-based generators. Denoted as pumping cycles, these flight patterns alternate between two distinct phases. The energy-generating traction phases, during which the tether forces are maximised by flying the wing in crosswind manoeuvres, and energy-consuming retraction phases, in which the tether forces are substantially reduced by reducing the angle of the wing with respect to the relative flow, allow for the reeled out tether to be retracted.

The analysis of Loyd<sup>1</sup> reveals that the achievable traction power depends quadratically on the aerodynamic lift-to-drag ratio  $L/D$  of the flying device and linearly on its lift coefficient  $C_L$ . The resulting cubic dependency on  $C_L$  has motivated the use of high-lift wings to maximise the net power per pumping cycle. As the tether force is generally orders of magnitude larger than the actual weight of the wing, AWE systems are exposed to substantially higher wing loading as compared with conventional aircraft. On the other hand, a low weight of the wing is crucial for performance of the system because it determines the cut-in wind speed.<sup>2</sup> The lighter the wing is, the lower the minimum wind speed at which the system can

-----  
This is an open access article under the terms of the Creative Commons Attribution-NonCommercial License, which permits use, distribution and reproduction in any medium, provided the original work is properly cited and is not used for commercial purposes.

© 2020 The Authors. Wind Energy Published by John Wiley & Sons, Ltd.

operate, further increasing the influence of the airborne mass on site specific yield — especially in low-wind operating conditions. Considering wind is a stochastic property and varies in magnitude and direction, a lower cut-in wind speed increases the annual yield and reduces the required number of landings and re-launches of the wing, further influencing the site-specific Levelized Cost of Electricity (LCOE) of the system.<sup>2,3</sup>

On the basis of the structure of the kite, AWE systems are commonly classified into “soft” or fabric based kites, and “rigid” kites. Soft kites are traditionally composed of woven fabric with additional stiffened sections to maintain an aerofoil shape. These stiffened sections are often composed of inflated tubes. The highly flexible nature of fabric kites makes the Fluid Structural Interaction (FSI) a field of active research. The structural model typically considered for soft kites consists of finite element models, where the canopy is discretised with shell elements and the reinforcements tubes (in the case of Leading Edge Inflated [LEI] kites) modelled with Euler beam elements.<sup>4,5</sup> Alternatively, the membrane canopy and inflated tubes can be modelled as an elementary cell, which is then modelled as an equivalent beam. These equivalent beams are then joined using virtual rigid bodies to account for the flexibility of the soft kite.<sup>6</sup> Rigid AWE systems normally utilise a more conventional aircraft-type configuration, with fuselage and wing combination.<sup>7</sup> These AWES commonly utilise carbon or glass fibre composites structures on account of their high strength-to-weight ratio. Rigid AWES kites typically achieve higher lift ratios than soft kites, and at nominal operation conditions are subjected to typical wing loading an order of magnitude higher than conventional aircraft wings as previously mentioned.

In contrast to the other “rigid” kites, EnerKite utilise lightweight, high-lift kites with large wing surface areas to fulfil design and power yield requirements. Figure 1 illustrates the 30-kW prototype EnerKite wing in crosswind flight and during assembly, in the workshop. The kite is composed of a carbon composite skeleton, with a textile polymer covering. To further improve yield, the power harnessing factor is enhanced by employing fixed leading edge slats to obtain a high lift coefficient  $C_L$ . These typical design choices at EnerKite require the wing to provide a traction force of well over 100 kg/m<sup>2</sup>, while maintaining a structural wing mass of  $\leq 3$  kg/m<sup>2</sup>. The desired low airborne mass of the system further influences and motivates the utilisation of a rotating mast based landing and launching system at EnerKite, as it requires minimal additional airborne mass.<sup>8</sup>

These demanding structural requirements have to be taken into account during the design of the wing and can only be achieved by a rigorous optimisation process. Right from the initial design stage, it is hence crucial to analyse and model the kite structure, especially given the deflection load coupling commonly witnessed in slender composite structures. Three-dimensional solid or shell-based finite element analysis of such composite structures requires detailed knowledge of geometry, properties of the laminate material, and fibre orientation, and moreover is computationally expensive. Particular to AWE, there has been some recent work on the analysis and optimisation of rigid composite kites, with the focus on morphing wings.<sup>9</sup> However, this kind of detailed analysis, given the computational costs involved, is uncommon in the initial iterative design stage. An alternative methodology would be to model the kite structure as an equivalent composite beam, while accounting for the unconventional wing-box topologies by determining characteristic 2D cross-sectional stiffness while taking into account the varied shape and composite lay-up along the span.<sup>10</sup>

Unlike traditional aircraft wings and wind turbine blades that utilise a rectangular torsion box at quarter-chord, the kite structure under consideration utilises an atypical “D” shaped wing-box, henceforth referred to as the D-box, and is illustrated in Figure 2. The D-box comprises an aerofoil shaped “C” shell section, and a vertical web and flange section. The increased weight penalty from utilising a rectangular torsion box, along with additional reinforcements at the leading edge for the high-lift devices and tether attachments, motivates this atypical wing-box shape. The lightweight construction utilises the wing-box along with composite ribs and a textile covering to maintain the aerodynamic shape of the wing.

This paper is structured as follows. In Section 2, we outline the physics of tethered flight with a focus on the unique swept wing as used by EnerKite. The methodology of structural model is outlined in Section 3. Details of the implementation of a composite cross section modeller is explained in Section 3.2, and the finite element composite beam model in Section 3.3. An overview of the methodology utilised to determine the aerodynamic and bridle loads for the structural model is described in Sections 3.4 and 3.5, respectively. This computational model of the kite is then utilised in an typical initial design configuration evaluation in Section 4, with an emphasis on exploring the effects of bridle configurations in Section 4.1 on the structural response. This is followed by a much more detailed mass minimisation of the D-box structure by tailoring the composite thickness and fibre orientation as outlined in Section 4.2.

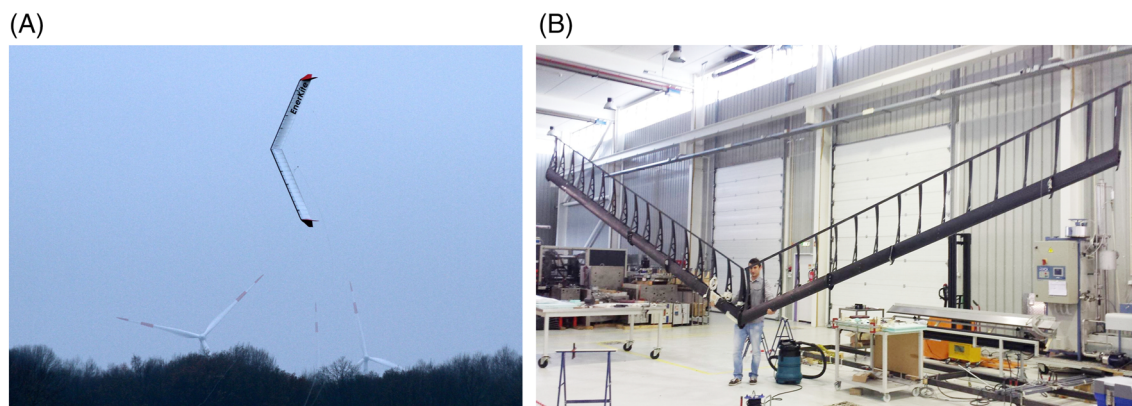


**FIGURE 1** A, EnerKite prototype wing during flight; B, wing skeleton in the workshop during assembly (right)<sup>53</sup>

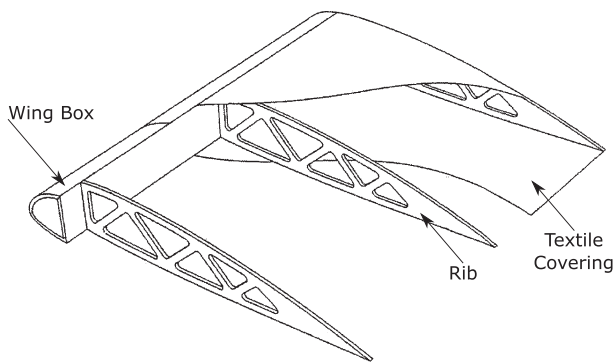


**FIGURE 2** Typical AWE EnerKite rigid kite wing structure illustrating the D-box, ribs, and textile covering

## 2 | FLIGHT DYNAMICS AND AEROELASTICITY OF BRIDLED WINGS

Compared with a traditional wind turbines, AWES, depending on their topology, have either “kite-like” or “conventional aircraft-like” flight dynamics. In addition, the presence of the tethered support to the ground introduces a force of equal magnitude of the aerodynamic forces under normal cross wind operation that needs to be accounted for. In this section, typical control strategies for common AWES topology are outlined. Particularly, the EnerKite tri-tether, bridled swept wing concept is detailed.

Flexible membrane wings do not have active control surfaces and are controlled via the warping/deformation of the flexible C-shaped wing. This allows for the control of the yawing and pitching motion of the kite – by utilising the entire wing as an aerodynamic actuator. The actual actuation for this control is achieved either via multiple lines directly from the ground station (EnerKite prototype ram air wing<sup>11</sup>), or an airborne control unit that directly manipulates the bridle lines (Skysails,<sup>12</sup> TU Delft/Kitepower). In the case of an airborne control unit, steering is achieved either by wing-tip warping or by the differential actuation of the wing-tip bridle lines, leading to the roll of the lift vector. This steering mechanism has an inherent disadvantage – it has also been observed that the control inputs (magnitude and frequency) have an impact on the material property of the flexible membrane, thus impacting the lifetime.<sup>12</sup>

The conventional rigid AWE wings with empennage concept use aerodynamic control surfaces, similar to conventional aircraft, for steering and power/depower control. Examples of this concept currently employed by the industry are Makani, TwingTec, Ampyx Power, etc.<sup>13,14</sup> As with conventional aircraft, to increase the effectiveness of the control surfaces, they are placed far away from the centre of rotation in order to increase the lever arm (flaps at the wing tips and rudder plus elevator on a tail plane). Bridling this wing constrains, the six rigid body Degree Of Freedoms (DOFs) and the deformation of the wing to a certain degree, depending on the bridle layout.<sup>15</sup>

The EnerKite wing modelled here in contrast consists of a tail-less high aspect ratio swept wing as already introduced in Figure 1. This bridled, swept rigid wing utilises a mix of both of the above concepts for control. Similar to the membrane kite, the kite is steered not via aerodynamic actuators but through manipulation of the tethers. The system is controlled from the ground, via three tether lines – two steering lines and one main power line. The EnerKite wing has no onboard control surfaces or actuators. The tail-less design of the wing attains the required pitch damping and stability by planform design (wing sweep, washout, dihedral, etc) as well as by manipulating the resultant centre of aerodynamic pressure by 2D aerodynamic profile design and obtaining the desired static stability by suitable bridling. This concept is described in further detail subsequently.

A schematic representation of pitch and roll control achieved by the manipulation of the tether lengths is seen in Figure 3. The reference zero pitch and roll configuration is shown in Figure 3A. Here, the datum positions of the three tether are also marked across all figures to serve as a visual reference. A pitch up manoeuvre is achieved by a symmetric reeling in of the control lines, while arresting the main line. This is visualised in

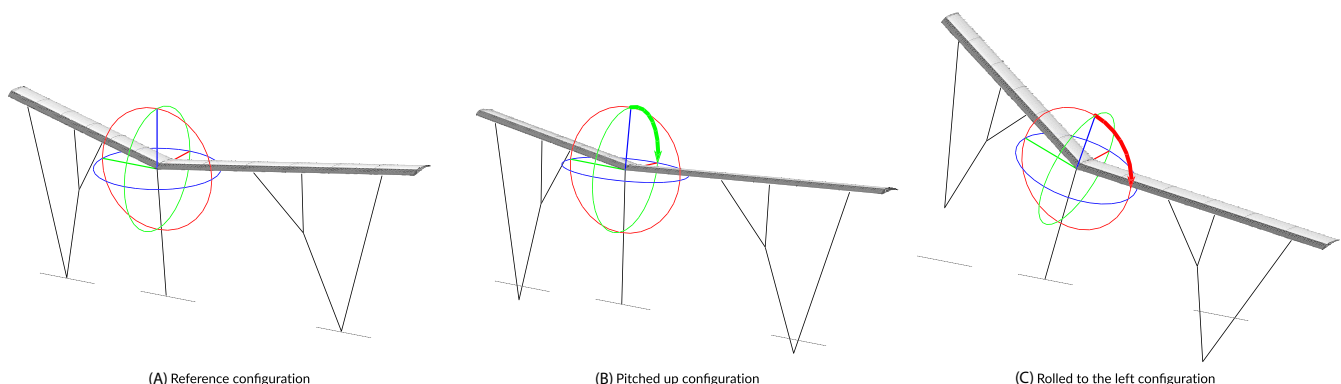


**FIGURE 3** Control of tri-tether rigid kites

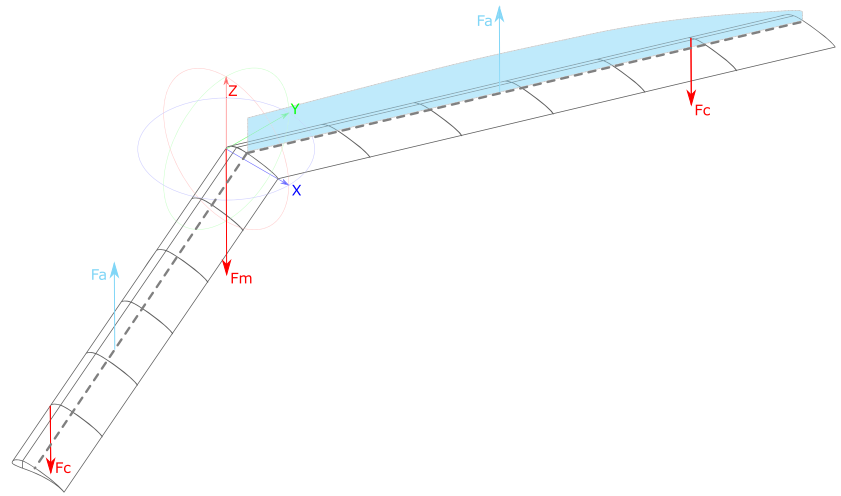


**FIGURE 4** Schematic of the tether and aerodynamic forces utilised for pitch and roll actuation

Figure 3B. Similarly, a rolling manoeuvre is achieved by an asymmetric actuation of the control lines, with the main line fixed again. This is seen in Figure 3C.

The differential actuation of the two steering lines causes the lift vector (aligned perpendicular to the airspeed and parallel to the tethers) to roll, thus resulting in a net effect akin to rolling in a conventional aircraft. For such ground actuated wings, control effectiveness is highly influenced by bridling positions relative to the aerodynamic centre of pressure. For effective pitch control, the longitudinal stability is determined from the resultant force  $F_m$  of the main line and the forces  $F_c$  of the control lines along with the aerodynamic centre of pressure, and centre of gravity of the wing as depicted in Figure 4. As can be seen from the illustration, the effect of planform of the wing plays a significant part in the stability. Depending on the spanwise ( $YX$  plane) location of the tether attachment point, there is a coupled effect on both the lateral and longitudinal stability of the wing. This is naturally further influenced by the chordwise ( $ZX$  plane) location of the attachments. It should be further noted, there is an additional challenge for control – as the tethers transmit no compressive forces, and can only transfer tensile forces.

When looking at aeroelastic phenomenon of AWES systems, the aeroelastic phenomenon of bridled membrane kites has been studied extensively, given their conventional use as parachutes.<sup>16,17</sup> Considering explicit AWES usage, fluid structure interaction studies commonly model the reinforced tubes and struts as rigid multibody elements, with the tensile membrane modelled as crosswise spring elements that connect these rigid bodies.<sup>5,18</sup> This structural model is then subjected to a spanwise, local aerodynamic load that is modelled as a function of the aerofoil and local angle of attack. Three-dimensional aerodynamic effects are thus neglected in such a model.

Swept wings demonstrate unique aeroelastic phenomenon such as aileron reversal and geometric coupling. Furthermore, the load deflection coupling in composites can lead to structural failure. An example of such phenomenon was seen recently in a high aspect ratio swept carbon composite wing – the Aquila 1A Unmanned Air System (UAS). A combination of gusts, upward deflected elevons, and low angle of attack lead to a negative lift component, resulting in torsion that further lead to downward deformation and ultimately leading to the failure of the wing-box.<sup>19</sup>

The light weight rigid structures utilised in AWES are subjected to larger average wing loading than a comparatively sized conventional aircraft wing as already mentioned. This is attributed to the prolonged maneuverer loads witnessed in typical crosswind flight performed by AWES wings. However, the bending and torsional forces on the wing can be alleviated by distributing the load introduction points by means of the bridling. The bridle allows for multiple load transfer points from the tether to the wing structure. The positions of the bridle attachment to the wing structure greatly influence both the static and dynamic structural response.<sup>20</sup> During these crosswind manoeuvres, the resultant aerodynamic loads are equivalent in magnitude to the resultant bridle forces acting on the entire wing section at every time instant considered. For the EnerKite ground steered tri-tether swept wing concept, the span and chordwise attachment positions of the bridles with respect to the aerodynamic moment determines both the control authority and the distribution of the forces between the main and the control lines as just described. The position of bridle under the wing also significantly effects the structural response of the wing and is explored in more detail in Section 4.

### 3 | COMPUTATIONAL MODEL

The structural response of the kite can be broadly defined as a function of wing geometry, material properties, and external loading. We first discuss typical external loads subjected on the wing for AWE systems, before outlining the modelling methodology employed here. The external loads on the wing are decomposed into the aerodynamic loads and the loads stemming from the bridle system attached under the wing. Figure 5 illustrates a typical tri-tethered swept wing AWES. The bridle system that attaches at multiple points under the wing is also depicted. The spanwise aerodynamic lift distribution is indicated in blue, and the forces arising from the bridle attachment by red vectors along the bridle lines under the wing. The body-fixed wing reference frame  $XYZ$  is also introduced and has its origin at wings nose, ie, the leading edge of the root profile.

The external loads acting on the equivalent kite structural model during typical operation is illustrated in Figure 6. The aerodynamic forces and moments acting on the wing are obtained from the spanwise aerodynamic lift distribution depicted in blue in Figure 6A. The methodology utilised

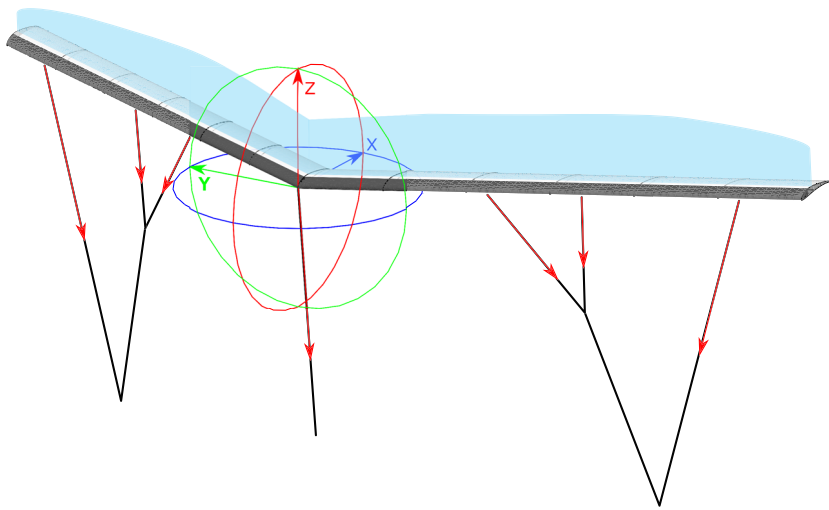


**FIGURE 5** Typical tri-tethered bridled swept wing for AWE, with aerodynamic and bridle loads

to determine these loads is discussed in more detail in Section 3.4. It should be noted that chord wise location of the aerodynamic forces need not coincide with the location of the D-box. Figure 6B depicts the bridle forces that are determined from the bridle system and the aerodynamic loads. The methodology utilised to model the system of pulleys and lines of the bridle is detailed in Section 3.5.

The first simplification that the model makes is to only consider the load bearing member of the wing – the D-box, neglecting addition structural members such as the ribs and the textile covering. The external loads are then applied on the D-box as depicted in Figure 6C. The strains and corresponding deflections of the structure can then be expressed as a function of the applied loads, cross section geometry, laminate properties, and composite lay-up of the D-box. The 3D slender composite D-box shell structure is further reduced to a 2+1D representation. This is achieved by discretising the D-box into characteristic 2D cross sections that are arranged along the span of the wing. These 2D cross sections are utilised to derive stiffness characteristics that are then utilised in a 1D beam model to capture the 3D structural response of the D-box. This 2+1D reduction of the three-dimensional kite structure is depicted in Figure 7. A beam reference frame  $xyz$  is introduced and has its origin at the

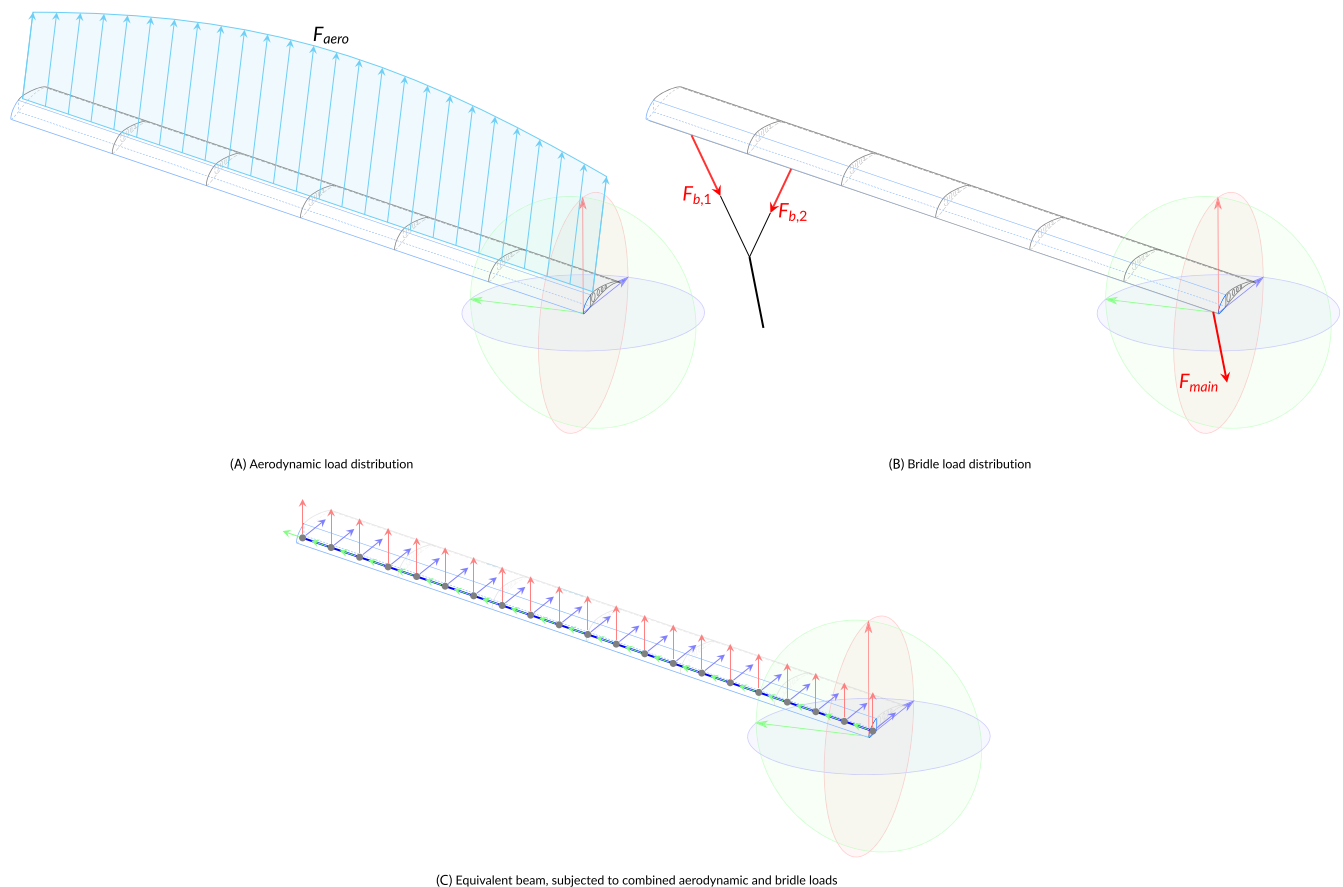


**FIGURE 6** Application of external loads on equivalent kite structural model

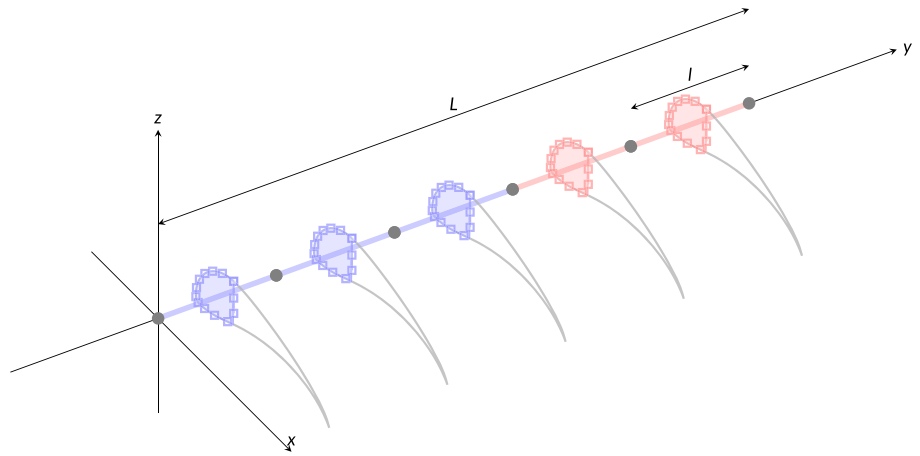
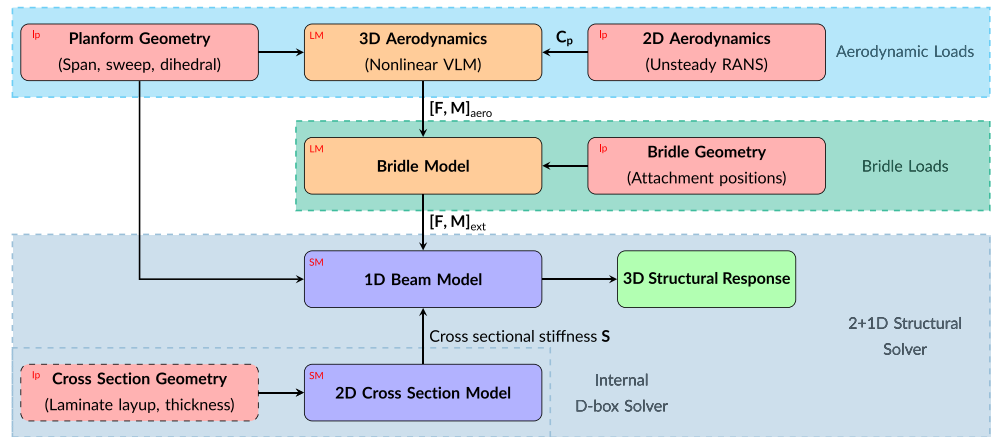


**FIGURE 7** 2+1D representation of the kite structure

**FIGURE 8** Functional kite structural model overview. All model inputs indicated in red boxes and shorthand **Ip**. External load models are indicated in orange boxes and shorthand **LM**, and structural models are indicated in purple boxes and shorthand **SM**



root of the beam. The  $y$ -axis of this frame is aligned along the axis of the beam. Here,  $L$  is the length of the one-dimensional beam, and  $l$  is the length of each one-dimensional element.

Each one-dimensional beam element is characterised by a cross-sectional stiffness. This stiffness is a function of the two-dimensional cross-sectional geometry, the laminate lay-up, and internal wall thickness, and as depicted in Figure 7, and can be different at each element. Thus, the two-dimensional model captures the geometry and lay-up of the cross section, and the one-dimensional model captures the planform geometry of the wing, such as span, sweep, and dihedral.

An overview of all the modules incorporated into the computational model is provided in Figure 8. The inputs and corresponding outputs are outlined, as well the hierarchy and interdependencies of the modules illustrated. The model allows for the selection of the desired level of fidelity during different stages of the design analysis. The inputs to the structural model are broadly broken down into wing planform parameters and cross-sectional geometric parameters as just described. At the current design stage, the wing planform (span, sweep, washout, dihedral) along with the 2D aerodynamic profiles are frozen. The 2D aerodynamic profiles are then utilised by the 3D nonlinear VLM described in Section 3.4 to obtain the spanwise 3D aerodynamic loads for the given aerodynamic profile and wing planform. These aerodynamic loads are utilised along with the bridle model described in Section 3.5 to determine the bridle loads and thus obtain the external loads acting on the structure.

### 3.1 | Structural modelling of composite kite wings

Composite materials by nature of their anisotropy tend to have a lower ratio of shear to extension modulus when compared with isotropic materials. Thus, in the analysis of slender composite structures, it is critical to capture the shear deformation effects — as compared with a geometrical equivalent isotropic beam. Compared with the well known Euler-Bernoulli beam model, the Timoshenko beam model is based upon first-order shear deformation theory and includes transverse shear effects but neglects the effects of cross-sectional warping and transverse normal strains. Hence, given the use of composites, in order to capture the tension-shear coupling, we utilise a Timoshenko-based beam element to model the 1D planform aspect of the wing. An added advantage is the ability of calculating the Timoshenko stiffness matrix about an arbitrary reference point, thus neglecting the requirement of calculation of the shear centre explicitly for each design iteration.

Asymmetric cross sections along with varied lamination stacking sequences, introduce coupling effects in slender composite structures between extension, bending and torsional stiffness, leading to bend-twist and extension-twist couplings.<sup>21</sup> In order to account for these, beam elements that consider these anisotropic effects need to be utilised. From beam elements that include shear effects in literature, different methods have been utilised to consider the effects of material anisotropy. Stemple and Lee developed an element that directly utilises the laminate

stiffness matrix ( $\mathbf{ABD}$ ) and incorporates shear effects by prescribing warping displacements parallel to deformed axis that are then superimposed over the cross section.<sup>22</sup> Saravanos et al formulate a shear beam element for hollow, closed cross sections, with an arbitrary skin laminate lay-up, with a focus on capturing the damping effects of the composite lay-up.<sup>23</sup> Kim et al formulated an element that with an arbitrary higher order polynomial displacement assumption, followed by minimising the elastic energy of the entire beam to obtain a solution.<sup>24</sup> Kennedy et al use a homogenisation-based theory that expresses the stress and strains as a linear combination of the solution of pre-chosen solutions shapes, along with the contribution from the strain residual that accounts for the solution parts not captured by the fundamental solution.<sup>25</sup> They also exist higher order beam models, based on the variational asymptotic method (VAM)<sup>26</sup> and unified Carrera one-dimensional formulation<sup>27,28</sup> that utilise higher-order shear deformation theory.

Given the aim of incorporating this kite wing structural model in an optimisation framework, for use during the initial design stage, a trade off is sought between computational cost, model parameter knowledge, and accuracy. Motivating the implementation of a Timoshenko beam element that can utilise an arbitrary cross section and laminate lay-up, that captures the geometric and anisotropic coupling effects from the arising fully populated Timoshenko stiffness matrix, while neglecting higher-order shear deformation effects. The element formulation is described in Section 3.3. Taking into account these coupling effects during analysis at this early design stage of the wing, allows for exploration of parameters to fine tune the structural behaviour, and gauge the effects of utilising these coupling effects for load alleviation and other aeroelastic phenomenon such as roll-reversal and flutter.<sup>29,30</sup>

### 3.2 | Kite wing cross section modelling

The D-box is a fibre reinforced composite structure that is built up from layers of laminae — where each individual lamina could theoretically be of different material and/or fibre orientations and thus as a whole exhibits anisotropic material properties. A typical cross section of the D-box with the individual layers is visualised in Figure 9A. Here, the individual lamina are depicted in different colours to indicate that each have different fibre orientations.

In order to obtain the cross-sectional stiffness properties of the structure, an anisotropic thin-walled cross section modeller developed by Ferede et al<sup>31</sup> is utilised. The 2D finite element model utilises linear Hermitian elements, to discretise the cross section, where each element takes into account the equivalent laminate geometry and stiffness. The process of discretising the layers of the cross section is visualised in Figure 9B, where each cross section element's stiffness needs to be prescribed. It is important to take into account the variation of the laminates stiffness as a function of the number and orientations of the layers of fibres in the laminate. A commonly utilised methodology to take this layer variation into account is Classical Laminate Theory (CLT) that allows for the determination of the in-plane, out-of-plane, and coupling stiffness parameters for each laminate stack up. The resulting stiffness matrix  $\mathbf{ABD}$ , is a symmetric  $6 \times 6$  matrix that relates the applied loads to the associated strains arising in the laminate. The notation  $\mathbf{A}$  is used for the in-plane component,  $\mathbf{D}$  for the out-of-plane component and  $\mathbf{B}$  for the coupling parameters.

The stiffness of laminate can be decomposed as a function of the material depended properties, and the individual fibre orientations of each lamina. This decoupling allows for the expression of the laminate stiffness using lamination parameters that allows for the expression of the

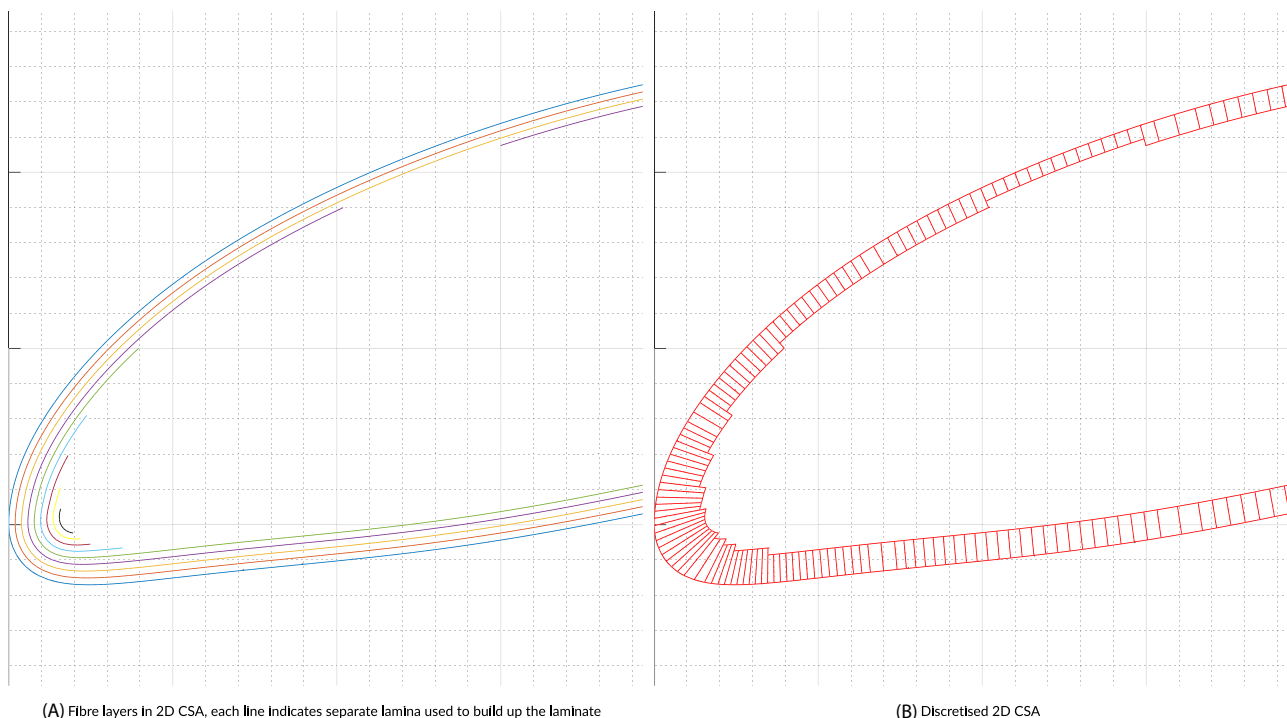


**FIGURE 9** Capturing geometry, laminate lay-up, and thickness from the 2D cross section

stiffness in terms of material invariants, and lay-up sequences. The material invariants  $\mathbf{U}$  as the name suggests considers the material properties of the laminate and is expressed as a function of the reduced stiffness matrix<sup>32</sup> of the unidirectional lamina  $\mathbf{Q}_{ij}$ :

$$\begin{aligned} U_1 &= (3Q_{11} + 3Q_{22} + 2Q_{12} + 4Q_{66})/8 \\ U_2 &= (Q_{11} - Q_{12})/2 \\ U_3 &= (Q_{11} + Q_{22} - 2Q_{12} - 4Q_{66})/8 \\ U_4 &= (Q_{11} + Q_{22} + 6Q_{12} - 4Q_{66})/8 \\ U_5 &= (Q_{11} + Q_{22} - 2Q_{12} + 4Q_{66})/8. \end{aligned} \quad (1)$$

Or more conveniently expressed in tensor form  $\Gamma_{0..4}$  as

$$\Gamma_0 = \begin{bmatrix} U_1 & U_2 & 0 \\ U_4 & U_1 & 0 \\ 0 & 0 & U_5 \end{bmatrix}, \quad \Gamma_1 = \begin{bmatrix} U_2 & 0 & 0 \\ 0 & -U_2 & 0 \\ 0 & 0 & 0 \end{bmatrix}, \quad \Gamma_2 = \frac{1}{2} \begin{bmatrix} 0 & 0 & U_2 \\ 0 & 0 & U_2 \\ U_2 & U_2 & 0 \end{bmatrix}, \quad \Gamma_3 = \begin{bmatrix} U_3 & -U_3 & 0 \\ -U_3 & U_3 & 0 \\ 0 & 0 & -U_3 \end{bmatrix}, \quad \Gamma_4 = \begin{bmatrix} 0 & 0 & U_3 \\ 0 & 0 & -U_3 \\ U_3 & -U_3 & 0 \end{bmatrix}. \quad (2)$$

Similarly, the effects of the laminate lay-up sequence are captured by the lamination parameters. The in-plane lamination parameters  $\xi^A$ , out-of-plane parameter  $\xi^D$  and coupling parameter  $\xi^B$  are then determined by

$$\begin{aligned} \xi_{[1,2,3,4]}^A &= \frac{1}{2} \int_{-1}^1 [\cos 2\theta(\bar{z}) \sin 2\theta(\bar{z}) \cos 4\theta(\bar{z}) \sin 4\theta(\bar{z})] d\bar{z} \\ \xi_{[1,2,3,4]}^B &= \int_{-1}^1 [\cos 2\theta(\bar{z}) \sin 2\theta(\bar{z}) \cos 4\theta(\bar{z}) \sin 4\theta(\bar{z})] \bar{z} d\bar{z} \\ \xi_{[1,2,3,4]}^D &= \frac{3}{2} \int_{-1}^1 [\cos 2\theta(\bar{z}) \sin 2\theta(\bar{z}) \cos 4\theta(\bar{z}) \sin 4\theta(\bar{z})] \bar{z}^2 d\bar{z} \end{aligned} \quad (3)$$

where  $\theta(\bar{z})$  is the laminate orientation distribution expressed as a function of the thickness normalised height  $\bar{z} = (2/h)z$ . Subsequently, the bending, extension, and coupling laminate stiffness tensors  $\mathbf{A}$ ,  $\mathbf{B}$ , and  $\mathbf{D}$  are then expressed as a linear combination of the material invariants  $\Gamma_{0..4}$  and the lamination parameters  $\xi^{A,B,D}$  just defined:

$$\begin{aligned} \mathbf{A} &= h (\Gamma_0 + \Gamma_1 \xi_1^A + \Gamma_2 \xi_2^A + \Gamma_3 \xi_3^A + \Gamma_4 \xi_4^A) \\ \mathbf{B} &= \frac{h^2}{4} (\Gamma_0 + \Gamma_1 \xi_1^B + \Gamma_2 \xi_2^B + \Gamma_3 \xi_3^B + \Gamma_4 \xi_4^B) \\ \mathbf{D} &= \frac{h^3}{12} (\Gamma_0 + \Gamma_1 \xi_1^D + \Gamma_2 \xi_2^D + \Gamma_3 \xi_3^D + \Gamma_4 \xi_4^D) \end{aligned} \quad (4)$$

The reasoning behind modelling the laminate stiffness using lamination parameters is motivated by the subsequent optimisation that is carried out using this computational framework. This is further detailed in Section 4.2.2. It is important to note although that from the perspective of the cross-sectional modeler, the methodology for the determination of the laminate stiffness is insignificant, and the motivation here is from the design optimisation problem that is formulated in Section 4.2.

Utilising the cross-sectional modeller, for each unique 2D cross section in the structure, the second-order fully populated  $6 \times 6$  Timoshenko stiffness tensor  $\mathbf{S}$  of the cross section is then determined by solving the shell kinematic variational asymptotic representations of the Saint Venant solutions.<sup>31</sup> This stiffness tensor relates the one-dimensional forces and moments acting on the beam to the experienced strains and curvatures as:

$$\mathbf{F} = \mathbf{S} \cdot \boldsymbol{\epsilon} \quad (5)$$

where  $\mathbf{F}$  is the cross-sectional load vector that comprises the forces and moments defined as

$$\mathbf{F} = \left\{ F_x, F_y, F_z, M_x, M_y, M_z \right\}^T \quad (6)$$

and the cross-sectional strain vector  $\boldsymbol{\epsilon}$  that similarly groups the strains and curvatures as

$$\boldsymbol{\epsilon} = \left\{ \epsilon_x, \epsilon_y, \epsilon_z, \kappa_x, \kappa_y, \kappa_z \right\}^T \quad (7)$$

The sectional stiffness  $\mathbf{S}$  takes into account transverse shear and is determined by minimisation of the sectional strain energy, using the Hamilton principle. By including the warping displacements, a fully populated Timoshenko stiffness tensor that takes into consideration all coupling effects is calculated. Furthermore, in the implemented modeller, the stiffness tensor  $\mathbf{S}$  is determined about any arbitrary reference point in the cross section — this negates the requirement of determining the shear centre and neutral axis a priori, which is critical during the optimisation of the cross-sectional geometry and lay-up that is detailed later in Section 4.2.

### 3.3 | Kite wing as a composite beam

To complement the implemented cross-sectional modeller just described in Section 3.2, a one-dimensional beam model is required. Here, a two node linear Timoshenko beam element with 12 (six translations and six rotations) degrees of freedom is formulated using the following relations. The described beam element considers the anisotropic material effects by utilising a fully populated  $6 \times 6$  sectional stiffness matrix for each element and includes the coupling effects that are commonly lost in standard Timoshenko beam elements that consider simplified flexural rigidity and torsional rigidity for a predefined cross section. Thus, an anisotropic composite or nonhomogeneous slender structure can be modelled, while imposing that the cross-section is constant for each element in the 1D analysis. At this juncture, only small deformations and strains are considered in a linear element formulation. The coordinate system utilised in the formulation of the element is shown in Figure 10A, where each element  $e$  has a characteristic stiffness tensor  $S_e$  and an element length  $l$ , and the overall length of the beam is define as  $L$ .

#### 3.3.1 | Constitutive equations and displacement field

The displacement field  $\mathbf{u}$  for each node can be expressed in terms of three translations ( $u_x, u_y, u_z$ ) and three rotations ( $\theta_x, \theta_y, \theta_z$ ) as illustrated in Figure 10B. The displacement field  $\mathbf{u}$  can thus be expressed as

$$\mathbf{u} = \{ u_x, u_y, u_z, \theta_x, \theta_y, \theta_z \}^T. \quad (8)$$

Similar to Equation (5), for each node, the generalised Timoshenko strain vector  $\epsilon$  that incorporates the effects of transverse shear can be expressed in terms of the elements of displacement field  $\mathbf{u}$  as

$$\epsilon = \{ \dot{u}_x - \theta_z, \dot{u}_y, \dot{u}_y + \theta_x, \dot{\theta}_x, \dot{\theta}_y, \dot{\theta}_z \}^T \quad (9)$$

Consecutively, from the Timoshenko relations, the translations are decomposed into the effects arising from shear stress, and those stemming from the bending moment and are expressed as

$$\begin{aligned} \frac{\partial u_x}{\partial y} &= \theta_z + \epsilon_{yx} \\ \frac{\partial u_z}{\partial y} &= -\theta_x + \epsilon_{yz} \end{aligned} \quad (10)$$

where  $\epsilon_{yx}$  and  $\epsilon_{yz}$  are the shear strains in the  $yx$  and  $yz$  planes, respectively.

#### 3.3.2 | Equilibrium and compatibility equations

For a cross-sectional applied load vector  $F$ , the equilibrium conditions for the shear stress and bending moment relations are given by

$$\begin{aligned} \frac{\partial M_x}{\partial y} - F_z &= 0 \\ \frac{\partial M_z}{\partial y} + F_x &= 0 \end{aligned} \quad (11)$$

From the principle of virtual work, the potential energy  $\Pi$  of a system can be defined as the sum of the strain energy  $U$  and work done by the external forces  $V$  and is expressed as

$$\Pi = U + V \quad (12)$$

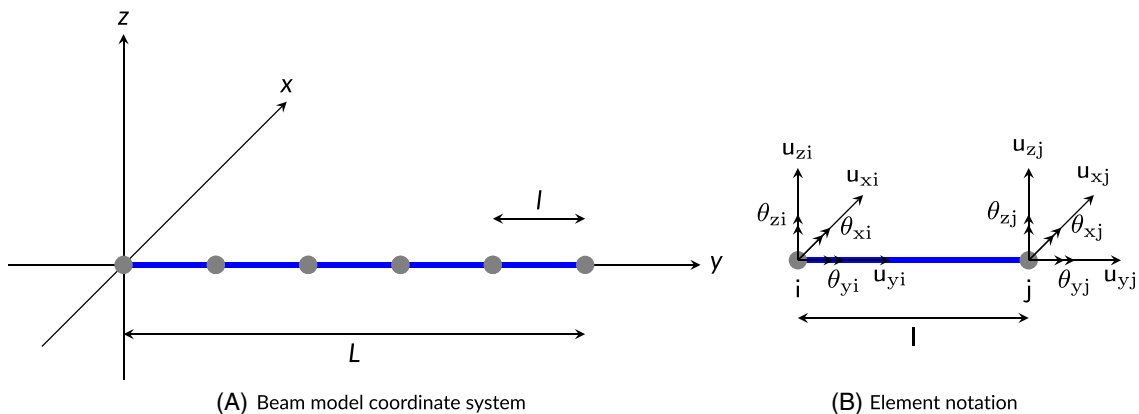


FIGURE 10 Beam element notation

where

$$\mathbf{U} = \frac{1}{2} \int_V \mathbf{F} \cdot \boldsymbol{\epsilon} dV \quad (13)$$

Thus, to attain equilibrium, the strain energy is minimised, ie,

$$\frac{\partial \mathbf{U}}{\partial \mathbf{u}} = 0 \quad (14)$$

### 3.3.3 | Finite element implementation

For the FE implementation, a two node element is considered as described previously, with its reference frame as defined in Figure 10A, and where each element has an elemental length  $l$ , depicted in Figure 10B. The displacement field for each of the 2 node are expressed as three translations and three rotations as similarly defined previously in Equation (8). Thus, the elemental displacement vector  $\mathbf{u}(\xi)$ , defined using the normalised element coordinate  $\xi = y/l$ , can given by

$$\mathbf{u}(\xi) = \mathcal{N}(\xi) \mathbf{u}_i \quad (15)$$

where  $\mathcal{N}(\xi)$  is the element shape function matrix and where the nodal displacement field  $\mathbf{u}_i$  is given for the element's  $i, j$  nodes by

$$\mathbf{u}_i = \{ u_{xi}, u_{yi}, u_{zi}, \theta xi, \theta yi, \theta zi, u_{xj}, u_{yj}, u_{zj}, \theta xj, \theta yj, \theta zj \}^T \quad (16)$$

In order to approximate the translations in the displacement field  $\mathbf{u}$ , following the kinematics of a beam undergoing bending,<sup>33</sup> a linear shape function is chosen for the axial displacement  $u_y$ , while cubic shape functions are chosen for the cross-sectional planar displacements  $u_x$  and  $u_z$ . For the rotations in the displacement field, a linear shape function is assumed for the torsional rotation along the beam axis  $\theta_y$ , and following the Timoshenko assumptions of Equation (10), the cross-sectional rotations are expressed as derivatives of the cross-sectional planar displacements ( $u_x$  and  $u_z$ ) along with an additional unknown each, to account for the shear deformation contributions  $\epsilon_{yx}$  and  $\epsilon_{yz}$ . This ultimately leads to 14 unknown coefficients for the beam element, which is expressed as the polynomial matrix  $\mathbf{A}$  presented subsequently in Equation (18). The shape function matrix  $\mathcal{N}(\xi)$  is subsequently built up from these displacement assumptions along with the compatibility and equilibrium conditions as

$$\mathcal{N}(\xi) = \mathbf{A}(\xi) \mathbf{E}(\xi)^{-1} \mathbf{T} \quad (17)$$

where  $\mathbf{A}(\xi)$  is the polynomial coefficient matrix consisting of the 14 unknowns from the displacement assumptions outlined previously and is given by

$$\mathbf{A}(\xi) = \begin{bmatrix} \xi^3 & \xi^2 & \xi & 1 & 0 & 0 & 0 & 0 & 0 & 0 & 0 & 0 & 0 & 0 \\ 0 & 0 & 0 & 0 & \xi & 1 & 0 & 0 & 0 & 0 & 0 & 0 & 0 & 0 \\ 0 & 0 & 0 & 0 & 0 & 0 & \xi^3 & \xi^2 & \xi & 1 & 0 & 0 & 0 & 0 \\ 0 & 0 & 0 & 0 & 0 & 0 & -3\xi^2 & -2\xi & -1 & 0 & 1 & 0 & 0 & 0 \\ 0 & 0 & 0 & 0 & 0 & 0 & 0 & 0 & 0 & 0 & 0 & \xi & 1 & 0 \\ 3\xi^2 & 2\xi & 1 & 0 & 0 & 0 & 0 & 0 & 0 & 0 & 0 & 0 & 0 & -1 \end{bmatrix} \quad (18)$$

The equilibrium and compatibility equations as outlined in Section 3.3.2 are then expressed as the coefficient matrix  $\mathbf{E}(\xi)$  and is cast in the form of the element equilibrium coefficients that are dependent on the normalised element coordinate  $\mathbf{E}_1(\xi)$  and the boundary displacement compatibility conditions  $\mathbf{E}_2$  that are only dependent on the element length  $l$ . The matrix  $\mathbf{T}$  in Equation (17) is a transformation matrix that accounts for the boundary compatibility conditions, ie,

$$\mathbf{E}(\xi) = \begin{Bmatrix} \mathbf{E}_1(\xi) \\ \mathbf{E}_2 \end{Bmatrix} \quad (19)$$

where

$$\mathbf{E}_2 = \begin{Bmatrix} \mathbf{A}(0) \\ \mathbf{A}(l) \end{Bmatrix} \quad (20)$$

The matrix  $\mathbf{E}_1$  is obtained by utilising the coefficient form of the equilibrium relations from Equation (11) and is expressed by casting the cross-sectional load vector  $\mathbf{F}$  components in terms of the elemental cross-sectional stiffness tensors  $\mathbf{S}$  (expressed in matrix notation), along with the nodal strain vector  $\boldsymbol{\epsilon}$  from Equation (9). The strain vector  $\boldsymbol{\epsilon}$  however is cast in the normalised element coordinate  $\xi$  using the displacement approximations from Equation (18) to yield

$$\mathbf{E}_1 = \begin{bmatrix} 6S_{46} - 6S_{36}\xi & -2S_{36} & 0 & 0 & -S_{23} & 0 & 6S_{34}\xi - 6S_{44} & 2S_{34} & 0 & 0 & -S_{33} & -S_{35} & 0 & -S_{13} \\ 6S_{66} + 6S_{16}\xi & 2S_{16} & 0 & 0 & S_{12} & 0 & -6S_{46} - 6S_{14}\xi & -2S_{14} & 0 & 0 & S_{13} & S_{15} & 0 & S_{11} \end{bmatrix} \quad (21)$$

Note the inclusion of off-diagonal coupling terms of the stiffness tensor  $\mathbf{S}$ , so as to include both geometric and material coupling effects in the beam element formulation. The strain displacement matrix is then obtained from the shape function matrix  $\mathcal{N}(\xi)$  defined in Equation (17) and

can be separated into a displacement component and its derivative term as

$$\mathbf{B}(\xi) = \mathbf{B}_0 \mathcal{N}(\xi) + \frac{\partial \mathcal{N}(\xi)}{\partial \xi} \quad (22)$$

where  $\mathbf{B}_0$  is a transformation matrix to account for the Timoshenko strains as defined in Equation (9).

From the displacement field, the strain field is expressed in terms of the strain displacement matrix  $\mathbf{B}(\xi)$  and the nodal displacements  $\mathbf{u}_i$  as

$$\epsilon = \mathbf{B}(\xi) \mathbf{u}_i \quad (23)$$

Thus, the element stiffness tensor  $\mathbf{K}_e$  is obtained by expressing Equation (13) with Equation (23) and numerically integrating along the element length  $l$  to get:

$$\mathbf{K}_e = \int_0^l \mathbf{B}(\xi)^T \mathbf{C} \mathbf{B}(\xi) d\xi \quad (24)$$

Care is taken to avoid shear locking by choosing the appropriate number of integration points along the elemental length. This implemented one-dimensional composite Timoshenko beam element is then coupled with the cross-sectional stiffness matrix obtained as described in Section 3 to complete the structural model of the kite. Utilising this model, the structural response of the wing is then determined by incorporating the external loads on the wing as described subsequently.

### 3.4 | Aerodynamic loads

For the analysis and subsequent optimisation, an indicative design load case of a typical reeling out cross wind manoeuvre is determined. In pumping cycle airborne wind energy systems, the power at the ground station is determined by the traction force generated by the kite in the tethers. This aerodynamic force is naturally then a function of the airspeed, angle of attack, and the glide ratio of the wing. The relationship for the available traction force is a function of the wing lift coefficient  $C_L$  and the system drag coefficient  $C_D$  and defined by the ratio  $C_L^3/C_D^2$  and thus a higher ratio is crucial for the power output from the wing.<sup>1</sup>

In aircraft systems, this design goal is known as minimum sink and leads to long airborne times at slow speeds, as well as the ability to take-off on short runways. For AWE systems, since the system drag additionally includes the drag of several hundred metres of tether that connect the kite to the ground, this puts an even higher emphasis on a high lift coefficient compared with other systems with this design goal, such as agricultural aircraft.

Hence, AWE wings operate constantly in a region where inviscid aerodynamic design methods fail to accurately model the decrease in lift slope with angle of attack, as well as the dramatic increase in drag stemming from these wings operating near the stall region. To take viscous effects at high angles of attack into account, (Reynolds-averaged) Navier-Stokes equations solvers or viscid-inviscid interaction methods<sup>34</sup> need to be employed. While two-dimensional methods are used routinely in the design and analysis of aerofoils, three-dimensional methods are currently too computationally expensive to use in the initial iterative wing design process. This is well described by C.P. van Dam<sup>35</sup> where the difficulties and trade-offs that have been made in the past regarding the common methods utilised to design high-lift systems are discussed. In addition, a method is presented by van Dam et al<sup>36</sup> that couples the results of two-dimensional aerodynamic calculations with a single-step Vortex Lattice Method (VLM). This method extends the use of nonlinear sectional lift data for simple lifting-line calculations, an idea that dates back to the 1940s.<sup>37</sup>

In more recent studies, nonlinear VLM has frequently been proposed for the calculation of aerodynamics of kites. Leloup et al present a lifting-line method, which differs from the vortex-lattice methods in placing the collocation points directly on the lifting line.<sup>38</sup> However, no nonlinear aerofoil behaviour is employed, besides the evaluation of the drag coefficient due to the effective angle of attack and Reynolds number, which then is subsequently utilised to derive the glide ratio. Dupont et al adapts this method to iteratively solve for the nonlinear aerofoil section lift data as well and compares it with RANS calculations.<sup>39</sup> Gaunaa et al<sup>40</sup> present a method similar to the one described by van Dam et al previously.

In these methods, a local effective angle of attack over the wingspan can be found from the flow direction and the downwash of all vortex elements. By changing the geometric twist such that the local lift from the vortex strength is equivalent to the viscous aerofoil lift at the effective angle of attack — disregarding the introduced geometric twist, the lift is reduced at high angles of attack. These methods are grouped under the term  $\alpha$ -methods to indicate the tailoring of the local effective angle of attack over the span.<sup>41</sup> In contrast to these  $\alpha$  methods, the term  $\Gamma$  methods could be used to describe a set of methods that do not change an effective angle of attack or twist but instead utilise different boundary conditions to achieve the same end goal. Compared with the  $\alpha$  methods, they are arguably better justified from a fluid-dynamics perspective, because they do not make ad-hoc changes to the angles of attack. However, they have been dismissed in the past due to concerns of convergence.<sup>41</sup>

The method used here is a  $\Gamma$  method which employs a fast Newton method to include the fully nonlinear boundary conditions and does not suffer convergence issues. It is based on the generalisation of the VLM boundary conditions, adapted for the nonlinear lift slopes as was initially proposed by Piszkin et al.<sup>42</sup> The complete details of the implementation can be found in Ranneberg,<sup>43</sup> which has since been adopted to be used in the National Renewable Energy Laboratory (NREL) AWE simulator.<sup>44</sup> Here, only the highlights of the method are briefly outlined subsequently.

### 3.4.1 | Linear vortex step boundary conditions

The classic linear vortex step method places horseshoe vortices along the quarter-cord line of the lifting surfaces that travel along the cord until the trailing edge and are aligned in the direction of the free flow.<sup>45</sup> Every vortex is assumed to be of constant strength, and the individual strength of each vortex is found by calculating the downwash of all vortices onto central collocation points at  $\frac{3}{4}$ -cord in every horseshoe and forcing a parallel flow condition.

The motivation of this choice comes from the two-dimensional analysis of inviscid flow over parabolic aerofoils. When modelled as a single vortex, the vortex needs to be located at the centre of pressure, which for flat plates and parabolic aerofoils is at quarter-cord. In addition, to arrive at the predefined two-dimensional inviscid lift-slope of  $2\pi$  the strength of this vortex must be chosen such that the downwash of this vortex leads to tangential flow at the  $\frac{3}{4}$ -cord. This condition is known as the Pistolesis theorem.

Using the above boundary conditions of the linear vortex step method is compatible with Pistolesis theorem in the sense that – for straight wings and an infinite aspect-ratio, the wing has a lift-slope of  $2\pi$  and a centre of pressure located at the quarter-cord.

### 3.4.2 | Nonlinear vortex step boundary conditions

While it is commonly stated that the boundary conditions of vortex lattice methods are derived from tangential flow conditions, as explained above the choice of collocation point and vortex position is an ad-hoc choice. For a large number of vortex lattice elements over the cord, the choice of collocation point and vortex position becomes increasingly less important – but for a single vortex the choice has significance. At every other collocation point, a single vortex will not lead to tangential flow if chosen by the above rule. At any position  $kc$  on the aerofoil, the downwash is given by

$$D_{2D} = \Gamma \frac{1}{4\pi c(k - \frac{1}{4})} \quad (25)$$

It is the compatibility with a  $2\pi$  lift-slope for infinite aspect-ratio wings as well as the general knowledge of the centre of pressure at the quarter-cord that motivates the boundary conditions.

Instead, we turn to Prandtl's Lifting-Line method.<sup>46</sup> There, the local angle of attack due to downwash motivates the choice of circulation directly by assuming a lift-slope for the local aerofoil, evaluated at the quarter-cord. Together with Kutta-Joukowski law, the evaluation of the local angle of attack leads to a system of equations that define the circulation strength:

$$\frac{\Gamma}{c} = C_{L,2D}(\alpha_0 - D_{3D}) \quad (26)$$

To generalise this idea to arbitrary collocation points in a way that is compatible with the two-dimensional case, we can add the two-dimensional downwash within this equation:

$$\frac{\Gamma}{c} = C_{L,2D}(\alpha_0 - D_{3D} + D_{2D}) \quad (27)$$

For the quarter cord, we still arrive at the lifting line method. For any other position on the cord, the three-dimensional and two-dimensional downwash are identical for an infinite wing and the two-dimensional aerofoil case is obviously compatible with the known two-dimensional lift slope. At the  $\frac{3}{4}$ -cord, assuming a linear lift-slope, we arrive at tangential flow conditions and thus the classic linear vortex step method, ie,

$$\frac{\Gamma}{c} = 2\pi \left( \alpha_0 - D_{3D} + \frac{\Gamma}{c} \right) \quad (28)$$

$$0 = \alpha_0 - D_{3D}. \quad (29)$$

## 3.5 | Bridle loads

A bridle in the context of AWE is the system of tether segments and pulleys under the kite that connects the structure of the wing to the tether(s). The bridles are responsible for distributing and transferring the aerodynamic loads on the wing to the tether(s) and ultimately the ground station.

As discussed earlier, the bridle configuration is an important aspect of the AWE system, as it influences both the load introduction for the structure, and the stability of the wing. Furthermore, for ground actuated AWE systems such as the EnerKite system, the controllability of the kite is governed by the choice of bridle system. A suitable bridle configuration along with three tethers results in a favourable load distribution along the wing that allows for the control of the EnerKite wing in both pitch and roll. With no control surfaces onboard the wing, the control principle can be compared to an aircraft which is steered by shifting its centre of gravity. In addition to controlling the kite, the bridling allows for the distribution of the load introduction over the wing, potentially allowing for the reduction of the wing's bending moment. Thus, the bridle system configuration is another aspect that can be tuned to obtain potential savings in the structural mass of the wing.

It is thus important to know the resulting forces due to the bridle system in order to determine the structural response of the wing. With every angle of attack and apparent wind speed, the forces and directions of the bridle changes to attain an equilibrium with the aerodynamic forces and moments. Tethers for AWE systems are routinely modelled as elastic spring elements,<sup>47</sup> while bridles, owing to their much shorter segments, are more commonly modelled as line elements.<sup>15,18</sup> For an AWE systems with a single tether, the bridle configuration typically consists of a “Y”-shaped branch with a single pulley.<sup>15,20</sup> The position of the pulley is constrained by the total length of the branches, which is made up of

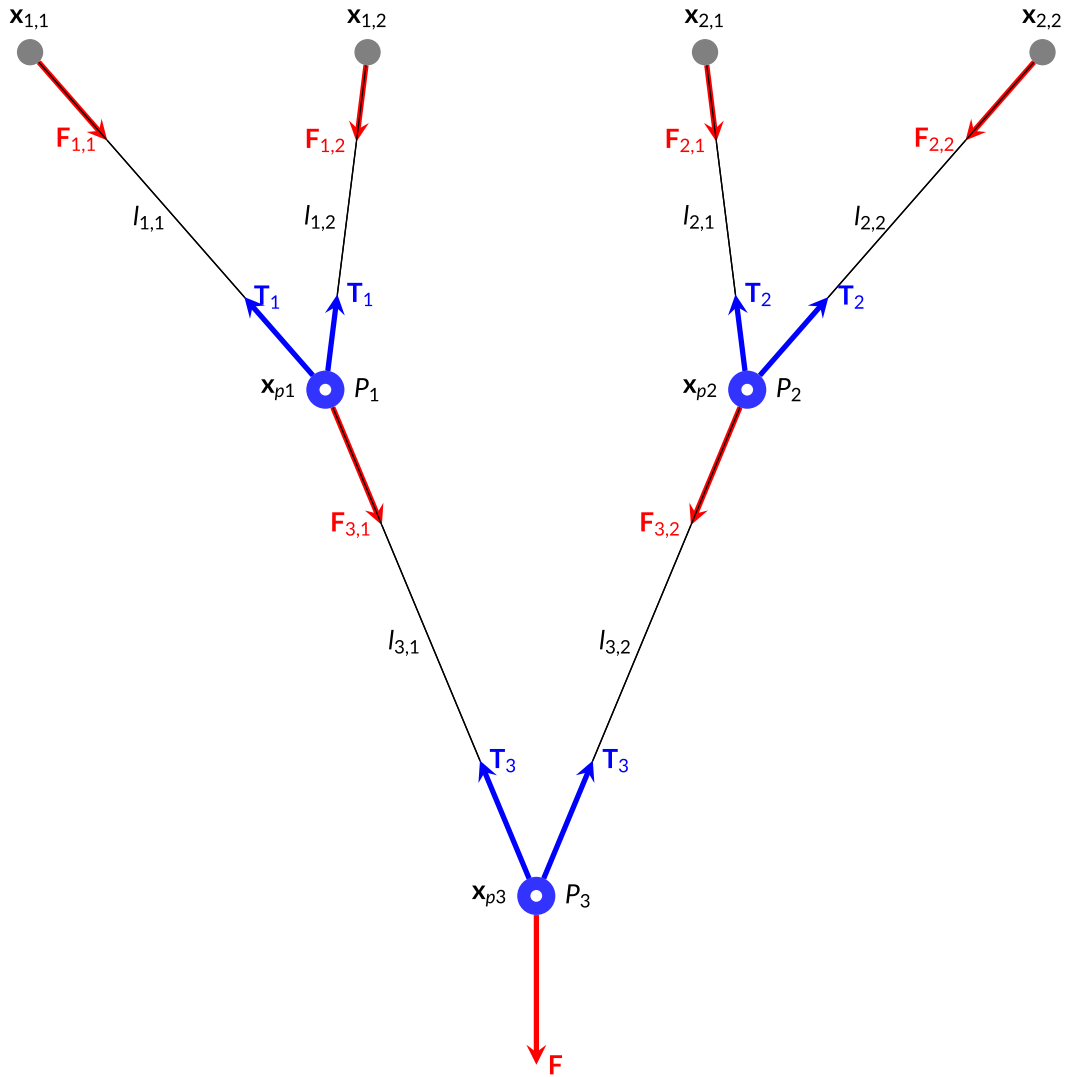


**FIGURE 11** Bridle system model notation, for a system of three pulleys ( $P_1, P_2, P_3$ ), and four attachment points  $x_{i,j}$

a single loop of tether. The length of the loop will deform and elongate due to tension in the tether loop that is in equilibrium with the force in the single tether segment leaving the pulley. When considering the dynamic system, the frictional coefficient of the pulley roller along with the velocity of the tether moving the pulley also influences the tension in the branches.

For a more complex system consisting of multiple pulleys, the bridle system can be described by a system of pulleys  $P_i$ , where the subscript  $i$  denotes the number of pulleys in the system. Each pulley at position  $X_p$  is subjected to a vector force  $F$  that is in equilibrium with the tension force in the branch that is composed of a loop of tether with a length  $L$ . The ends of the loop are attached at two points  $x_1, x_2$ . A bridle system with three such pulley systems ( $P_1, P_2, P_3$ ) is depicted in Figure 11.

Under nominal loading conditions, there is no sag in the tether segments, and thus, the forces at the two ends of the branch can be determined as a function of the tension in the lines and the position of the pulley. As we are interested only in the static loads at this stage of the analysis, neither the dynamic effects nor the effects of friction in the pulley system are considered currently. This allows for the pulleys to be modelled as points. Given that the bridle system is in static equilibrium with the aerodynamic forces, the short length of tethers in the branches of the system are modelled as rigid, closed line segments. The effects of the weight of the tethers and pulleys are considered negligible when considering magnitude of the aerodynamic forces. Furthermore, for the tri-tethered system described in this work, an additional constraint that all three tethers exiting the bridle system are parallel is imposed.

Thus, in equilibrium, the tether goes from  $x_1$  in a straight line to the pulley  $P$  at  $x_p$  and then to  $x_2$ . The tension in the tether leads to two forces on the pulley  $F_1, F_2$  which are in equilibrium with the force  $F$  acting on the pulley. The system of equations for a single pulley system can thus be described by:

$$F_1 = T \times \frac{x_1 - x_p}{\|x_1 - x_p\|} \quad (30)$$

$$F_2 = T \times \frac{x_2 - x_p}{\|x_2 - x_p\|} \quad (31)$$

$$F = F_1 + F_2. \quad (32)$$

If the attachment points  $x_1, x_2$  utilise another pulley again, the same situation occurs but  $F_1$  and  $F_2$  are the external forces on the new pulley, as in the case of the pulley system of  $P_3$  in Figure 11. This leads to a set of nonlinear equations where the unknowns are the pulley positions and the tether tensions, while the last external force of the system and the initial attachment points on the wing are known. The resulting set of equations is solved using a numerical method to arrive at the pulley positions and the forces at the attachment points arising from the external force. Thus, for each angle of attack and apparent wind speed, leading to the corresponding aerodynamic forces, a solution is obtained by setting the bridle forces in equilibrium with the aerodynamic forces. Together with the assumption of parallel tethers, this leads to a unique solution for the forces at the bridle attachment points at the wing.

## 4 | DESIGN AND OPTIMISATION PROCESS

With the computational model described, the procedure followed for an indicative wing structural design analysis is carried out. The first step would be to determine the design load case(s) for the wing. A typical crosswind maneuverer at a nominal wind speed is considered here, as the detailed selection of design load cases for AWES is outside the scope of the current discussion. For the aerodynamics, the 2D aerodynamic profile of the wing is obtained by an optimisation procedure that considers stability criteria required for the swept wing during both traction and retraction as described in Section 2. The resulting 2D aerodynamics characteristics is determined using unsteady RANS for the aerofoil profile considered. For the 3D wing, to keep computational costs low, the 3D aerodynamic loads are derived by the VLM method described in Section 3.4. At this stage, the analysis is carried out purely as a structural analysis and is not coupled with the aerodynamics. Hence, the aerodynamic loads are considered as static loads on the structure during the rest of the analysis. Thus, the remaining design space can be parameterised by two main factors:

1. Bridle configuration
2. 2D cross section properties

A typical design process that explores these two parameters with the current tool chain is described subsequently.

### 4.1 | Bridle configuration design

The computational model developed allows for the quick evaluation of this design space. To determine the influence of different bridle configuration, some typical bridle configurations explored at this stage of the design process are visualised in Figure 12. In the figure, the red force vectors indicate the force distribution at the attachment points along the wing structure. These examples were obtained by varying the design goal of the force distribution between the main and the control line. As discussed in Section 2, this force distribution between the three tethers play a vital role in the controllability of the swept wing.

Configuration A (Figure 12A) utilises a system of three pulleys for the main tether. Configuration B (Figure 12B) consists of a two pulley system, while configuration C (Figure 12C) utilises a single pulley system for each control tether. In both these configurations, the main line is attached directly. Configuration D (Figure 12D) consists of no pulleys while configuration E (Figure 12E) is a combination of configuration A and configuration C.

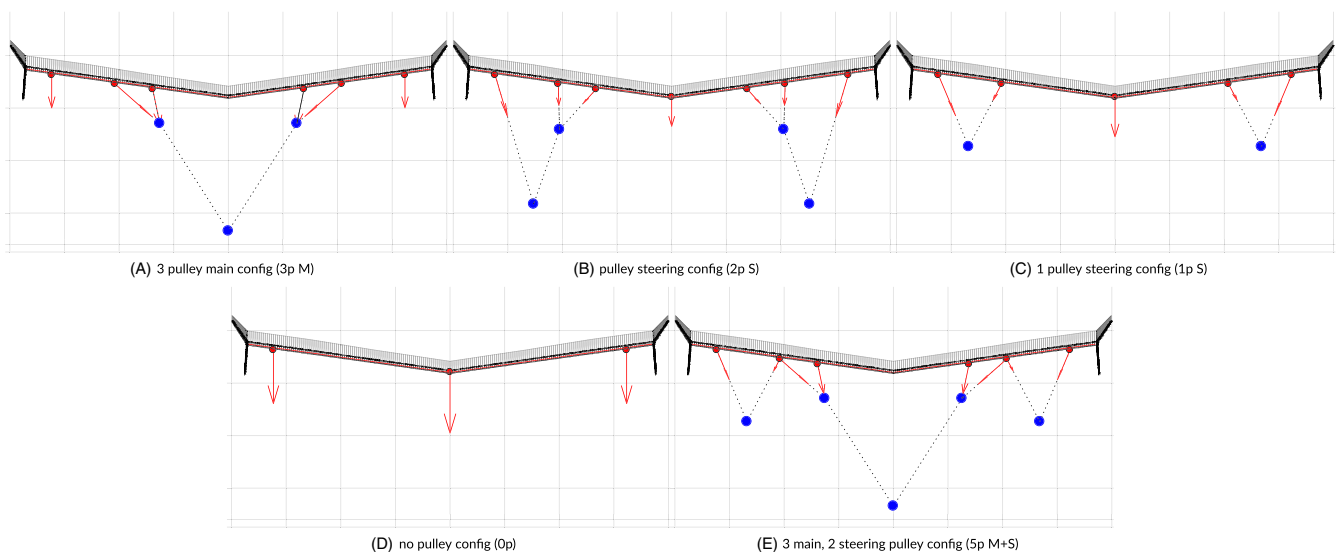


**FIGURE 12** Five indicative bridle configurations depicting the variation of bridle force distribution for same nominal cross wind operation design point

### 4.1.1 | Influence of the bridle on structures

The significance of the bridle configuration is further explored by analysing the structural response for the five bridle configurations A to E as illustrated in Figure 12. To better isolate and quantify the influence of the bridle configuration, wing planform and the 2D cross section geometry is fixed. This is done by denoting a reference stiffness tensor  $S_e$  for every element in the 1D model. This allows for a relative comparison of different bridle configurations, at the initial design stage without having to completely detail the laminate stack up and layout for the 2D cross section.

The cross-sectional geometry is considered in more details in the subsequent Section 4.2, for now it is sufficient to understand that in this case, two unique sections were considered along the span of the wing. Wherein two-thirds of the half span is composed of typical 2D sections described as root sections, and the rest of the span consists of 2D tip sections. These two sections were thus kept constant across all the bridle configurations considered at this stage of the analysis. Utilising the structural model, the resulting deflections are depicted in Figure 13.

The deflections in the figure are plotted in the beam reference frame  $xyz$  as introduced in Figure 5 that has its origin located at the half wing beam reference axis. While the change in the deflections due to the varying load distributions arising from the different bridle configurations is no surprise, the analysis methodology allows for the quantification of the effects. When comparing the magnitudes of deflection, the tip deflection is largest in the  $z$  axis, with the maximum deflection of  $\approx 5\%$  of the span as compared to  $\approx 1\%$  in the chordwise  $x$  axis and  $\approx 0.5\%$  for spanwise  $y$  axis.

When it comes to the deflections in the  $z$  axis, compared to traditional wings, the AWE D-box experiences downward wing tip deflections due the bridling. More bridle attachment points result in the reduction of the root bending moment, which results in lower  $z$  deflections for the configurations with more pulleys. It should be noted that from the structural point of view, more attachment points allow better load introduction, and thus lighter wings. However, the increase of the overall system drag needs to also considered.

## 4.2 | Internal structural optimisation

When considering the initial design parameter stage as described previously, the 2D cross-sectional geometry has a fixed outer profile determined a priori from the aerofoil shapes, derived from the aerodynamic requirements. This thus leaves the internal structural thickness and the laminate lay-up as variables in the design space. In order to optimise these, a mass minimisation is carried out, with the reference being the traditional CLT based initial design. The goal of this optimisation is to tailor the internal D-box geometry (fibre orientations and thickness) for a fixed external wing geometry (aerofoil, planform and bridle geometry), operating at a typical design load case. The details of the load case are unimportant in the scope of the current work, and are derived from nominal reel out loads from cross wind operation. Thus, structural mass is minimised by varying the thickness and fibre orientations, while maintaining a reference target stiffness that is prescribed by imposing a constraint on the allowable deflection of the structure.

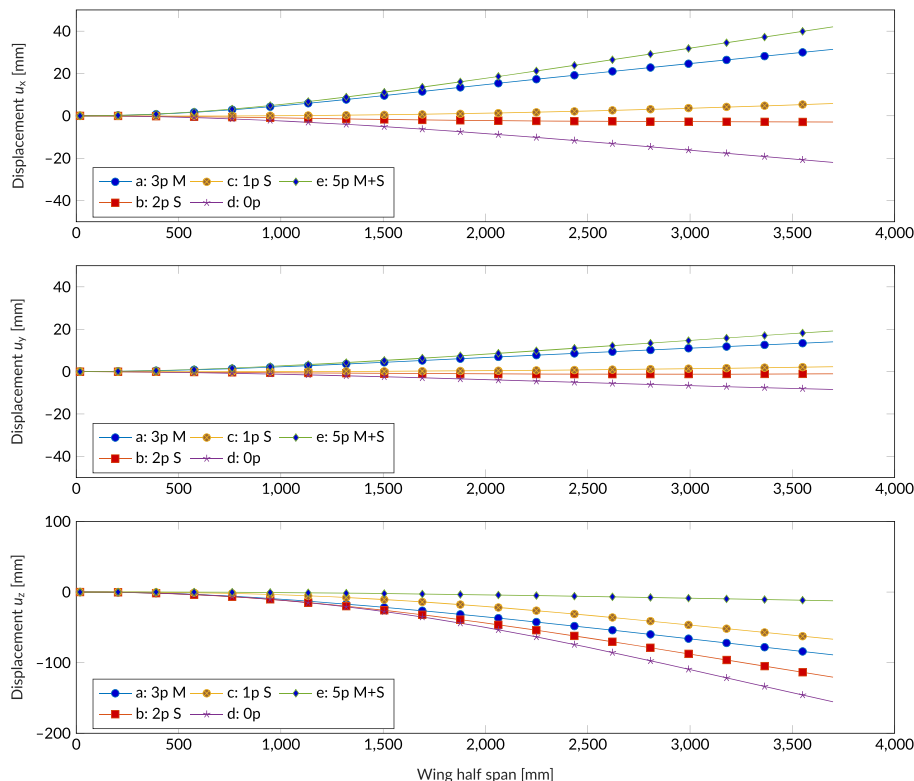


**FIGURE 13** Influence of bridle configurations on the structural response of typical wing box design. Note that the plot axes are not equal and are scaled

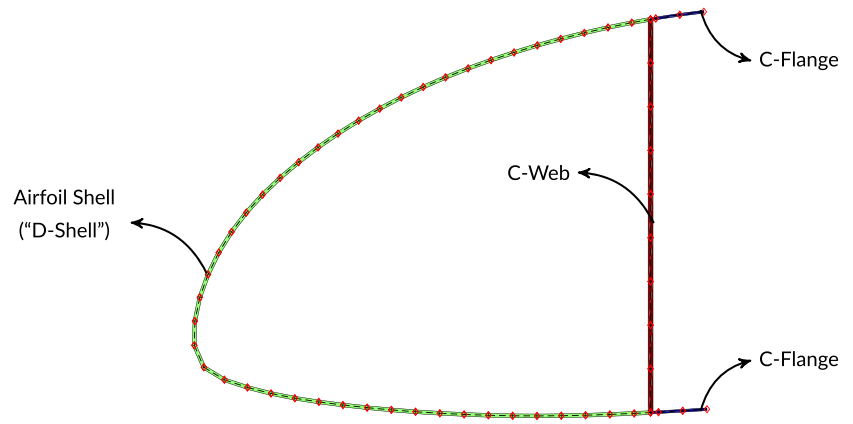


**FIGURE 14** Discretised D-box cross section, where each of the distinct geometric groups (D-Shell, C-Web, and C-Flange) have their own characteristic laminate lay-ups

#### 4.2.1 | Geometric parameterisation

In theory, the internal geometry of the D-box can be composed of any arbitrary laminate lay-up as illustrated in Figure 9A. However, when considering the typical manufacturing processes, the internal geometry of the D-box cross section can be deconstructed into a few geometrical groups. In this case, the internal geometry is broken down into a “C-Beam” and an aerofoil shaped shell “D-Shell” as illustrated in Figure 14. The “C-Beam” geometry is further composed of a single web and two flanges.

To aid in the manufacturing, each of these three geometric groups are composed of characteristic laminate lay-ups, ie, the fibre orientations and number of layers for every node in one of these geometric groups are maintained the same. This allows for the design space to be constrained according to the manufacturing process utilised during prototyping. Thus, for the optimisation considered, all two-dimensional elements in one geometric group are assigned the same thickness and characteristic stiffness properties. The characteristic stiffness for the laminate as indicated in Section 3.2 is a function of the material properties, as well as the fibre orientation in each individual layer of the laminate.

#### 4.2.2 | Lamination parameters

For each 2D node for the cross section solver, a characteristic stiffness parameter is required. For laminates, this is traditionally determined by Classical Laminate Theory (CLT) as touched upon in Section 3.2. In our current optimisation problem, we preselect our material properties based on manufacturing and availability criteria, but the overall thickness and fibre orientations for the layers in each geometric group are considered as optimisation variables. Hence, for every characteristic cross section in the wing, each distinct 2D geometric group will have a laminate stacking sequence, and thickness as variables for the optimiser.

In order to uncouple the dependency on the fibre angle orientations with the characteristic stiffness (**ABD**) of each 2D laminate node, lamination parameters are chosen over traditional CLT based **ABD** stiffness parameters. With lamination parameters, an arbitrary stacking sequence, with an arbitrary number of plies can be described by material invariants and 12 lamination parameters.<sup>48</sup>

Utilisation of lamination parameters greatly reduces the number of design variables of the optimisation problem, making the problem independent of the plies at each two-dimensional node. The second major advantage is that unlike the irregular, discrete ply angle design space of this manufacturing process, the lamination parameters design space is bounded and shown to be convex.<sup>49</sup> While closed form expressions for in-plane, out-of-plane and bending expressions for the case where they vary independently exist,<sup>50</sup> closed form solutions that completely constrain the entire feasible design space is still a topic of active research. To the authors knowledge, no closed form expressions are available for problems that are not strictly depended on either the in-plane stiffness or out-of-plane stiffness exclusively.

To determine a design space that utilises in-plane, out-of-plane, and coupling stiffness parameters, the feasible region is obtained by successive convex hull approximations leading to a large set of linear constraints (ie, 37126 for the fully coupled case).<sup>51</sup> For the current optimisation problem, the feasible region is determined from the convex hull for a set of ply angles chosen a priori following the methodology of Bloomfield et al<sup>52</sup> to suit the current manufacturing requirements, reducing the number of constraints.

#### 4.2.3 | Problem formulation

The aim of the optimisation problem is to minimise the mass of the D-box, while satisfying a predefined deflection criteria. In the problem, a baseline initial design is chosen from traditional CLT-based approximations. The mass of the D-box can be expressed a function of the individual thickness of each element, in each spanwise 2D cross section. As described in Section 4.2.1, each spanwise 2D cross section is broken down into three unique geometric groups – the D-Shell, C-Web, and C-Flange. Thus, for each 2D cross section, the elemental mass can be expressed as a function of the material density of the laminate, and the thickness profile of each of the three geometric element groups collected into the vector  $\mathbf{h}_i = [h_{shell}, h_{web}, h_{flange}]$ . Here, the subscript  $i$  denotes the index of the 2D cross section in consideration.

Thus, for the minimisation, the mass is computed as a function of the thickness profile of all 2D nodes, for all the 2D cross sections considered, and is represented by the vector  $\mathbf{h} = \mathbf{H}_1, \mathbf{h}_2, \dots, \mathbf{h}_n$ . Where  $n$  is the number of elements in the 1D model. The dimension of  $\mathbf{h}$  is thus the summation all the 2D nodes, for all the cross sections stacked along the span. Constraints on the maximum allowed deflections, laminate thickness, and the

	$\xi_{[1,2,3,4]}^A$	[-]
Stacking sequence	$\xi_{[1,2,3,4]}^B$	[-]
	$\xi_{[1,2,3,4]}^C$	[-]
Laminate thickness	$h$	[mm]

**TABLE 1** Optimisation variables for each of the three (D-Shell, C-Web, and C-Flange) two-dimensional element groups, leading to 39 variables for each characteristic two-dimensional cross section, and thus 78 variables in total for the two characteristic cross sections considered in the current optimisation

feasible design space for the lamination parameters are defined as follows:

$$\begin{aligned}
 &\text{minimize}_h \quad \sum_{i=1}^n M_i(h_i) \\
 &\text{subject to} \quad \mathbf{U}(\mathbf{h}) \leq \mathbf{U}(\mathbf{h})_{ref} \\
 &\quad \quad \quad \mathbf{h}_{min} \leq \mathbf{h} \\
 &\quad \quad \quad f(\xi^A, \xi^B, \xi^D) \leq 0
 \end{aligned} \tag{33}$$

where  $\mathbf{h}$  is a vector of the laminate heights of the shell, web and flange for all spanwise two-dimensional sections just described and  $\mathbf{U}$  is the deflection field of the D-box. For each two-dimensional geometric group, the design vector consists of 12 lamination parameters to account for the stacking sequence of the laminate, and one parameter for the laminate height  $h$  as described in Table 1. This leads to 39 variables for each 2D section that consists of three characteristic geometric groups (D-Shell, C-Web, and C-Flange) described in Figure 14.

For the current optimisation, the wing span is discretised into two characteristic 2D cross sections, the root and the tip 2D sections. As in earlier discussions in Section 4.1, two thirds of the beam span is composed of the root section, and the rest utilises the tip section. This leads to an overall design vector of 78 variables. A gradient-based interior point algorithm is utilised to solve the problem defined in Equation (33).

### 4.3 | Results and discussions

The example minimisation example problem for the two cross sections visualised in Figure 15 for the root cross section, and in Figure 16 for the tip cross section. In both figures, all thicknesses are plotted to scale, but are normalised to the initial reference design. Both sections are normalised to the thickness of the reference root section. This is done to reduce the effects of variation of the initial reference design in the reported results. This is important as the savings in the weight achieved is highly depended on the initial reference design, and the proximity of the initial reference design the cost function's minima.

The current cross section reference lay-up and thickness for the optimisation problem was determined utilising the calculation methodology typical employed during the initial design stages. The ‘‘C-Web’’ and ‘‘C-Flange’’ sections were sized using the critical forces and moments in the D-box. Classical laminated plate theory was then applied to size the corresponding thickness and lay-up for these sections along with the Tsai-Wu failure criteria.

From the results obtained, the benefits of utilising a more comprehensive design toolchain right from the initial design stage is seen. For the given laminate properties used in this analysis, the optimised laminate lay-ups lead to an overall  $\approx 20\%$  reduction in mass as compared with the initial reference cross section geometry. What is clearly apparent from the results is that the optimised profiles consider the contribution of the asymmetric aerofoil shell towards the stiffness of the D-box. Furthermore, in both the root and tip profiles, the lay-up in the ‘‘C-Web’’ and ‘‘C-Flange’’ sections are constrained to the minimum prescribed thickness defined the problem definition. For lay-ups in the tip section, an increase in the thickness of ‘‘D-Shell’’ is also witnessed. Given the deflection constraints imposed in the problem definition (Equation (33)), the optimised cross section profiles and laminate lay-ups show that it is possible to achieve similar overall torsional and edgewise stiffness with a smaller mass penalty from the optimised layout of the ‘‘D-Shell’’ as compared to initial thicker ‘‘C-Beam’’ sections.

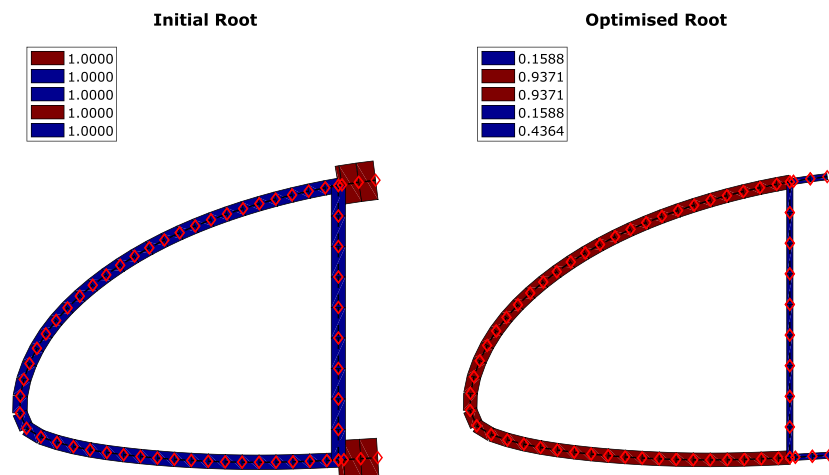


**FIGURE 15** Comparison of optimisation results for the root cross section. The element thicknesses illustrated are scaled to the actual laminate thickness

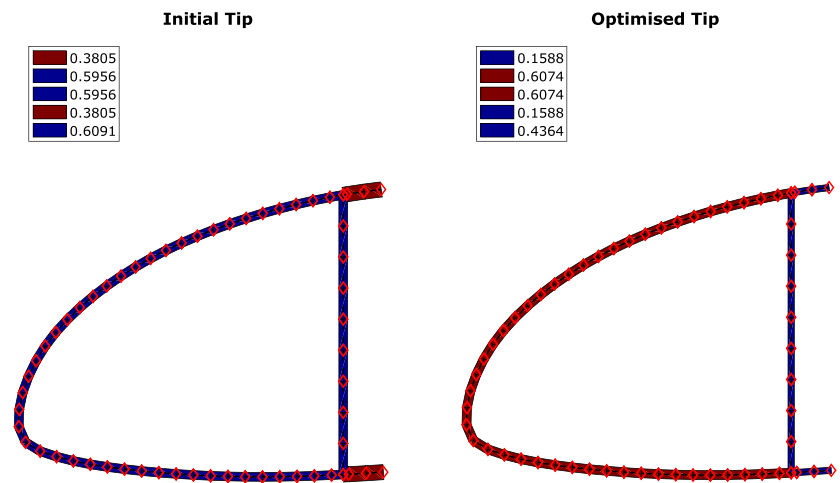


**FIGURE 16** Comparison of optimisation results for the tip cross section. The element thicknesses illustrated are scaled to the actual laminate thickness

## 5 | CONCLUSIONS

A methodology to idealise and model the structure of typical composite structures of rigid and semi rigid AWE kites is presented in this work. A computationally inexpensive structural model is developed that includes the effects of load coupling and other shear deformation effects experienced by slender composite structures, by modelling the main load bearing member of the composite kite with a 2+1D finite element approach. The wing-box in the particular case considered is an atypical D-box of the EnerKite rigid prototype swept wing that is modelled by considering individual 2D cross sections that are stacked along the span of an anisotropic 1D beam model. The external loads on the beam are determined using a nonlinear VLM for the aerodynamic loads, which is then coupled with a bridle model that determines the forces resulting from the bridle system at equilibrium conditions. This model allows for the computationally fast and inexpensive modelling of rigid composite kites for AWES applications.

The computational methodology developed allows for the exploration of the initial design space, utilising multiple levels of fidelity the 2+1D approach allows for. This is emphasised by comparing the influence of some typical bridle configurations on the deflections of the D-box, right at the initial design stage. This allows for the selection of a bridle configuration that meets both the stability and deflection design requirements prescribed, without having to detail the internal geometry and lamination lay-up of the wing-box.

Subsequently, utilising the external loads determined for the selected bridle configuration and the target deflection requirement, an optimisation of the internal geometry of a root and tip section of the EnerKite prototype swept rigid wing is carried out. The mass minimisation carried out yields in an optimised laminate lay-up and thickness that, for the typical load case evaluated, leads to an overall weight savings of  $\approx 20\%$  as compared with the initial reference design.

From the results, the motivation of analysing and optimising the kite structure right from the initial design stage is clear. From the perspective of the current implemented model, future work is ongoing to improve the current linear static beam model to incorporate the effects of large strains and deflections into the structural model, and couple the aerodynamic and bridle models to the structural model for fully coupled aeroelastic analysis.

## ACKNOWLEDGEMENTS

This work is supported by the project AWESCO (H2020-ITN-642682) funded by the European Union's Horizon 2020 research and innovation programme under the Marie Skłodowska-Curie grant agreement No. 642682. Roland Schmehl has received additional financial support by the project REACH (H2020-FTIPilot-691173), funded by the European Union's Horizon 2020 research and innovation programme under grant agreement No. 691173.

## CONFLICT OF INTEREST

The authors declare that they have no conflict of interest.

## ORCID

Ashwin A. Candade  <https://orcid.org/0000-0001-9228-1310>

Roland Schmehl  <https://orcid.org/0000-0002-4112-841X>

## REFERENCES

1. Loyd ML. Crosswind kite power. *J Energy Res.* 1980;4(3):106–111. <https://doi.org/10.2514/3.48021>
2. Ranneberg M, Brandt D, Bormann A, Rohde P, Breipohl F, Bastigkeit I. Fast Power Curve and Yield Estimation of Yo-Yo Airborne Wind Energy Systems. *Airborne Wind Energy – Advances in Technology Development and Research*. Green Energy and Technology. Singapore: Springer; 2018:77–95. [https://doi.org/10.1007/978-981-10-1947-0\\_25](https://doi.org/10.1007/978-981-10-1947-0_25)
3. Hussen K, Dietrich E, Smeltink J, et al. Study on Challenges in the commercialisation of airborne wind energy systems. ECORYS Report PP-05081-2016, Brussels: European Commission; 2018. <https://doi.org/10.2777/87591>
4. Bosch A, Schmehl R, Tiso P, Rixen D. Nonlinear Aeroelasticity, Flight Dynamics and Control of a Flexible Membrane Traction Kite. *Airborne Wind Energy, Green Energy and Technology*. Springer; 2013:307–323. [https://doi.org/10.1007/978-3-642-39965-7\\_17](https://doi.org/10.1007/978-3-642-39965-7_17)
5. Bosch A, Schmehl R, Tiso P, Rixen D. Dynamic nonlinear aeroelastic model of a kite for power generation. *AIAA J Guid Control Dyn.* 2014;37(5):1426–1436. <https://doi.org/10.2514/1.G000545>
6. de Solminihac A, Nème A, Duport C, et al. Kite as a Beam: A Fast Method to get the Flying Shape. *Airborne Wind Energy – Advances in Technology Development and Research, Green Energy and Technology*. Singapore: Springer; 2018:77–95. [https://doi.org/10.1007/978-981-10-1947-0\\_4](https://doi.org/10.1007/978-981-10-1947-0_4)
7. Cherubini A, Papini A, Vertechy R, Fontana M. Airborne wind energy systems: a review of the technologies. *Renew Sustain Energy Rev.* 2015;51:1461–1476. <https://doi.org/10.1016/j.rser.2015.07.053>
8. Rieck B, Ranneberg M, Candade A, Bormann A, Skutnik S. Comparison of Launching & Landing Approaches. In: *The International Airborne Wind Energy Conference 2017*. Book of Abstracts, University of Freiburg | Delft University of Technology; 2017. <http://resolver.tudelft.nl/uuid:746d1263-9685-452a-b26b-d26b6a138c65>
9. Fasel U, Keidel D, Molinari G, Ermanni P. Aerostructural optimization of a morphing wing for airborne wind energy applications. *Smart Mater Struct.* 2017;26(9):95043. <https://doi.org/10.1088/1361-665X/aa7c87>
10. Candade A, Ranneberg M, Schmehl R. Structural Analysis and Optimization of an Airborne Wind Energy System. In: *The International Airborne Wind Energy Conference 2017: Book of Abstracts*, University of Freiburg | Delft University of Technology; 2017. <http://resolver.tudelft.nl/uuid:d801586f-063b-4c54-8e3a-db411a295344>
11. Bormann A, Ranneberg M, Kövesdi P, Gebhardt C, Skutnik S. Development of a three-line ground-actuated airborne wind energy converter. *Airborne Wind Energy, Green Energy and Technology*. Berlin Heidelberg: Springer; 2013:427–436. [https://doi.org/10.1007/978-3-642-39965-7\\_24](https://doi.org/10.1007/978-3-642-39965-7_24)
12. Paulig X, Bungart M, Specht B. Conceptual Design of Textile Kites Considering Overall System Performance. *Airborne Wind Energy, Green Energy and Technology*. Berlin Heidelberg: Springer; 2013:547–562. [https://doi.org/10.1007/978-3-642-39965-7\\_32](https://doi.org/10.1007/978-3-642-39965-7_32)
13. Ahrens U, Diehl M, Schmehl R. *Airborne Wind Energy Green Energy and Technology*. Berlin Heidelberg: Springer; 2013. <https://doi.org/10.1007/978-3-642-39965-7>
14. Luchsinger R, Aregger D, Bezard F, et al. Pumping Cycle Kite Power with Twings. *Airborne Wind Energy – Advances in Technology Development and Research, Green Energy and Technology*. Singapore: Springer; 2018:603–621. [https://doi.org/10.1007/978-981-10-1947-0\\_24](https://doi.org/10.1007/978-981-10-1947-0_24)
15. Terink EJ, Breukels J, Schmehl R, Ockels WJ. Flight Dynamics and Stability of a Tethered Inflatable Kiteplane. *J Aircr.* 2011;48;2:503–513. <https://doi.org/10.2514/1.C031108>
16. Chatzikonstantinou T. Numerical analysis of three-dimensional non rigid wings. *10th Aerodynamic Decelerator Conference*. 1989. <https://arc.aiaa.org/doi/pdf/10.2514/6.1989-907>
17. Takizawa K, Tezduyar TE. Computational methods for parachute fluid–structure interactions. *Arch Comp Methods Eng.* 2012;19(1):125–169. <https://doi.org/10.1007/s11831-012-9070-4>
18. Breukels J, Schmehl R, Ockels W. Aeroelastic Simulation of Flexible Membrane Wings based on Multibody System Dynamics. *Airborne Wind Energy, Green Energy and Technology*. Berlin Heidelberg: Springer; 2013:287–305. [https://doi.org/10.1007/978-3-642-39965-7\\_16](https://doi.org/10.1007/978-3-642-39965-7_16)
19. National Transportation Safety Board. Pilot/Operator Aircraft Accident/Incident Report. NTSB Form 6120.1, Washington, DC: NTSB; 2017. <https://dms.ntsb.gov/public/59000-59499/59416/598766.pdf>
20. Wijinja J, Schmehl R, Breuker R, Jensen K, Vander Lind D. Aero-elastic analysis of a large airborne wind turbine. *J Guid Control Dyn.* 2018;41(11):2374–2385. <https://doi.org/10.2514/1.G001663>
21. Chandra R, Stemple AD, Chopra I. Thin-walled composite beams under bending, torsional, and extensional loads. *J Aircr.* 1990;27(7):619–626. <https://doi.org/10.2514/3.25331>
22. Stemple AD, Lee SW. A finite element model for composite beams undergoing large deflection with arbitrary cross-sectional warping. *Int J Numer Methods Eng.* 1989;28(9):2143–2160. <https://doi.org/10.1002/nme.1620280911>
23. Saravanos DA, Varelis D, Plagianakos TS, Chrysochoidis N. A shear beam finite element for the damping analysis of tubular laminated composite beams. *J Sound Vib.* 2006;291(3-5):802–823. <https://doi.org/10.1016/j.jsv.2005.06.045>
24. Kim T, Hansen AM, Branner K. Development of an anisotropic beam finite element for composite wind turbine blades in multibody system. *Renew Energy*; 59:172–183. <https://doi.org/10.1016/j.renene.2013.03.033>
25. Kennedy G, Martins J. A Regularized Discrete Laminate Parametrization Technique with Applications to Wing-Box Design Optimization. In: *53rd AIAA/ASME/ASCE/AHS/ASC Structures, Structural Dynamics and Materials Conference*, American Institute of Aeronautics and Astronautics; 2012. <https://doi.org/10.2514/6.2012-1519>
26. Yu W, Hodges DH, Volovoi V, Cesnik CES. On Timoshenko-like modeling of initially curved and twisted composite beams. *Int J Solids Struct.* 2002;39(19):5101–5121. [https://doi.org/10.1016/S0020-7683\(02\)00399-2](https://doi.org/10.1016/S0020-7683(02)00399-2)
27. Carrera E, Giunta G, Nali P, Petrolo M. Refined beam elements with arbitrary cross-section geometries. *Comput Struct.* 2010;88(5-6):283–293. <https://doi.org/10.1016/j.compstruc.2009.11.002>
28. Carrera E, Petrolo M. Refined one-dimensional formulations for laminated structure analysis. *AIAA J.* 50;1:176–189. <https://doi.org/10.2514/1.J051219>

29. Eastep FE, Tischler VA, Venkayya VB, Khot NS. Aeroelastic tailoring of composite structures. *J Aircr*. 1999;36(6):1041–1047. <https://doi.org/10.2514/2.2546>
30. Guo S, Cheng W, Cui D. Aeroelastic tailoring of composite wing structures by laminate layup optimization. *AIAA J*. 2007;44(12):3146–3150. <https://doi.org/10.2514/1.20166>
31. Ferede E, Abdalla M. Cross-sectional modelling of thin-walled composite beams. In: In: no. January in 55th AIAA/ASME/ASCE/AHS/ASC Structures, Structural Dynamics, and Materials Conference:1–16, American Institute of Aeronautics and Astronautics; 2014. <https://doi.org/10.2514/6.2014-0163>
32. Kaw A. *Mechanics of Composite Materials Mechanical Engineering Series*. 2nd ed. Boca Raton, FL: CRC Press; 2005. <https://doi.org/10.1201/9781420058291>
33. Przemieniecki JS. *Theory of Matrix Structural Analysis*. New York: SE; 468. illustrations 23 cm: McGraw-Hill; 1967.
34. Drela M. XFoil: An Analysis and Design System for Low Reynolds Number Airfoils. *Low Reynolds Number Aerodynamics, Lecture Notes in Engineering*, Vol. 54. Berlin-Heidelberg: Springer; 1989:1–12. [https://doi.org/10.1007/978-3-642-84010-4\\_1](https://doi.org/10.1007/978-3-642-84010-4_1)
35. Dam CP. The aerodynamic design of multi-element high-lift systems for transport airplanes. *Prog Aerosp Sci*. 2002;38(2):101–144. [https://doi.org/10.1016/S0376-0421\(02\)00002-7](https://doi.org/10.1016/S0376-0421(02)00002-7)
36. Dam CP, Vander Kam JC, Paris JK. Design-oriented high-lift methodology for general aviation and civil transport aircraft. *J Aircr*. 2001;38(6):1076–1084. <https://doi.org/10.2514/2.2875>
37. Sivells JC, Neely RH. Method for calculating wing characteristics by lifting-line theory using nonlinear section lift data. NACA Technical Note 1269, Langley, VA, USA, Langley Memorial Aeronautical Laboratory; 1947. <http://www.dtic.mil/dtic/tr/fulltext/u2/a801339.pdf>
38. Leloup R, Roncin K, Bles G, Leroux J-B, Jochum C, Parlier Y. Estimation of the Lift-to-Drag Ratio Using the Lifting Line Method: Application to a Leading Edge Inflatable Kite. *Airborne Wind Energy*. Berlin, Heidelberg: Springer Berlin Heidelberg; 2013:339–355. [https://doi.org/10.1007/978-3-642-39965-7\\_19](https://doi.org/10.1007/978-3-642-39965-7_19)
39. Dupont C, Deberque M, Leroux J-B, Roncin K, Jochum C. Local results verification of a 3D non-linear lifting line method for fluid-structure interactions simulation on a towing kite for vessels. *High-Perform Mar Veh*. 2017:79–97. [https://doi.org/10.1007/978-981-10-1947-0\\_4](https://doi.org/10.1007/978-981-10-1947-0_4)
40. Gaunaa M, Paralta CPF, Réthoré P-EM, Sørensen NN. A computationally efficient method for determining the aerodynamic performance of kites for wind energy applications, 18. <https://doi.org/10.1002/we.1757>; 2011.
41. Gallay S, Ghasemi S, Laurendeau E. Sweep effects on non-linear Lifting Line Theory near Stall. In: 2014 <https://doi.org/10.2514/6.2014-1105>
42. Piszkin ST, Levinsky ES. Nonlinear lifting line theory for predicting stalling instabilities on wings of moderate aspect ratio; 1976.
43. Ranneberg M. Direct Wing Design and Inverse Airfoil Identification with the Nonlinear Weissinger Method. arxiv:1501.04983 [physics.flu-dyn]:1–13. <https://arxiv.org/abs/1501.04983>; 2015.
44. Damiani R, Wendt FF, Jonkman JM, Sicard J. A Vortex Step Method for Nonlinear Airfoil Polar Data as Implemented in KiteAeroDyn. In: 2019 <https://doi.org/10.2514/6.2019-0804>
45. Katz J, Plotkin A. *Low-Speed Aerodynamics Cambridge Aerospace Series*, 2 ed. Cambridge: Cambridge University Press; 2001. <https://doi.org/10.1017/CBO9780511810329>
46. Prandtl L. Tragflügeltheorie IM. Nachrichten von der Gesellschaft der Wissenschaften zu Göttingen, Mathematisch-Physikalische Klasse. 1918;1918:451–477. <https://eudml.org/doc/59036>
47. Fechner U, Vlught R, Schreuder E, Schmehl R. Dynamic model of a pumping kite power system. *Renew Energy*. 2015;83:705–716. <https://doi.org/10.1016/j.renene.2015.04.028>
48. Tsai SW, Hahn HT. Introduction to composite Westport CT: Technomic Pub.; 1980.
49. Diaconu CG, Sato M, Sekine H. Feasible region in general design space of lamination parameters for laminated composites. *AIAA J*. 2002;40(3):559–565. <https://doi.org/10.2514/3.15097>
50. Hammer VB, Bendsøe MP, Lipton R, Pedersen P. Parametrization in laminate design for optimal compliance. *Int J Solids Struct*. 1997;34(4):415–434. [https://doi.org/10.1016/S0020-7683\(96\)00023-6](https://doi.org/10.1016/S0020-7683(96)00023-6)
51. Setoodeh S, Abdalla M, Gurdal Z. Approximate Feasible Regions for Lamination Parameters. In: In: Proceedings of 11th AIAA/ISSMO Multidisciplinary Analysis and Optimization Conference, American Institute of Aeronautics and Astronautics; 2006. <https://doi.org/10.2514/6.2006-6973>
52. Bloomfield MW, Diaconu CG, Weaver PM. On feasible regions of lamination parameters for lay-up optimization of laminated composites. *Proc R Soc A: Math Phys Eng Sci*. 2009;465(2104):1123–1143. <https://doi.org/10.1098/rspa.2008.0380>
53. Aircraft Design Certification GmbH. AD&C Project EnerKite/ATALOG. <http://www.aircraftdc.de/en/projects/80-enerkite-atolog.html>

**How to cite this article:** Candade AA, Ranneberg M, Schmehl R. Structural analysis and optimization of a tethered swept wing for airborne wind energy generation. *Wind Energy*. 2020;1–20. <https://doi.org/10.1002/we.2469>